University of Zurich[UZH]

June 25, 2021

Angular Analysis of Baryonic $\Lambda_b^0 \to \Lambda_c^+ \mu^- \bar{\nu}_\mu$ Decay at LHCb

Bachelor's Thesis

Author
Helena Kühnle

Supervisors
Prof. Nicola Serra
Dr. Patrick Owen
Dr. Abhijit Mathad
Martina Ferrillo

Abstract

In this analysis the effects of binning schemes and model variations on the Monte Carlo fits to Wilson Coefficients in the data of baryonic decays at the Large Hadron Collider beauty (LHCb) experiment are studied. As a consequence, systematic uncertainties due to a specific choice in the binning scheme and model can be assessed and the analysis strategy further improved.

Contents

Introduction **1**

1 Theoretical Concepts **1**
1.1 The Standard Model . . . 1
1.2 Search for New Physics . . . 2
1.3 Wilson Coefficients . . . 3
1.4 Form Factors . . . 4

2 LHCb Experiment **5**
2.1 Detector . . . 5
2.2 Trigger . . . 5
2.3 Particle Tracking . . . 6
2.4 Particle Identification . . . 7

3 Analysis Framework **10**
3.1 Phase Space . . . 10
3.2 Differential Decay Density . . . 10
3.3 Monte Carlo simulations . . . 11
3.3.1 Toy Models . . . 11

4 Binning Scheme Analysis **12**
4.1 Sensitivity Analysis . . . 12
4.2 Selection of Binning Schemes . . . 12
4.3 Binning Scheme Comparison . . . 13

5 Model Dependency Analysis **18**
5.1 Scenario Definition . . . 18
5.2 Weight Definition . . . 19
5.3 Model Dependent Scenario Comparison . . . 19

Conclusion **21**

Acknowledgements **22**

Appendix **23**

References **35**

Introduction

The search for new fundamental principles in physics has gained more and more importance during the last decades. The Large Hadron Collider beauty (LHCb) experiment detector at CERN is one of the main experiments addressing the search for New Physics (NP). In this thesis a binning as well as an efficiency and resolution analysis of the fits on Wilson coefficients in the decay of $\Lambda_b^0 \to \Lambda_c^+ \mu^- \bar{\nu}_\mu$ are presented.

The thesis will be structured in the following way:

- Chapter 1: the theoretical foundations of this thesis will be presented.
- Chapter 2: the LHCb experiment in terms of its components will be introduced.
- Chapter 3: the phase space, the underlying differential decay density as well as the generation of Monte Carlo toy models will be explained.
- Chapter 4: the binning scheme analysis will be presented.
- Chapter 5: the model dependency analysis will be introduced.

Later, the conclusions of the analysis are combined and the thesis is completed with a section for acknowledgements, the appendix and the list of references, figures and tables.

1 Theoretical Concepts

1.1 The Standard Model

The Standard Model (SM) combines the theories of the fundamental particles and describes their interactions. It describes how the particles interact under the influence of three of the four fundamental forces: the electromagnetic, the weak and the strong force, apart form the gravitational force. A schematic summary of the particles in the SM is given in Fig. 1.

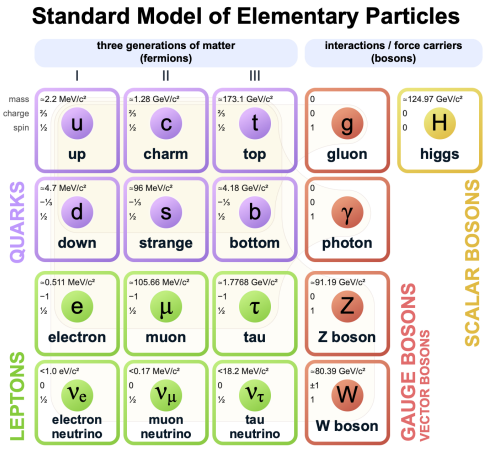

Figure 1: The Standard Model of elementary particles.

According to the SM, matter consists of so-called fermions, which are themselves divided into three generations of quarks and leptons being spin $\frac{1}{2}$-particles. There exist six quarks: the up (u), down (d), bottom (b), charm (c), strange (s) and top (t) quark with increasing masses in this order and either $+\frac{2}{3}$ or $-\frac{1}{3}$ charge. To every fermion, there exists an anti-fermion being oppositely charged. Particles involved in weak interaction processes, as quarks and gluons, carry a so-called color charge. This property is referred to as red, green and blue as well as their anti-colors anti-red, anti-green and anti-blue. Quarks can only exist in neutral color states, such as rgb, $\bar{r}\bar{g}\bar{b}$ or $c\bar{c}$ states, which partially explain quark confinement. Consequently, quarks are not stable by themselves and are observed either in $q\bar{q}$ particles, called mesons, or qqq respectively $\bar{q}\bar{q}\bar{q}$ particles, called baryons. Leptons are divided into the negatively charged electron (e), muon (μ), tau (τ)

and their corresponding neutral and lighter neutrinos (ν_e, ν_μ, ν_τ). The different types of leptons are referred to as flavours. Ref. [1]

The particles which describe the interactions or act as force carriers are spin 1-particles called gauge bosons: the massless and neutrally charged gluons ($g_1, ..., g_8$) correspond to the strong force acting between either quarks or each other. They are as well as the quarks carrying colour charge in eight possible combinations being described through a SU(3) symmetry. The neutrally charged and massless photon (γ) is carrying the electromagnetic force between charged particles. The fact that this mediator is massless explains the infinite interaction range because of the mass being inversely proportional to the interaction distance of the force. The Z^0 and $W^\pm$ bosons correspond to the weak force interaction with quarks and leptons as well with each other. These are the only bosons having a mass and in the case of $W^\pm$ bosons carrying charge. Because of the mediators being exceptionally heavy with $\sim 91\text{GeV/c}^2$ and $\sim 80\text{GeV/c}^2$ respectively (Ref. Fig. 1), the weak interaction is short-ranged. The electroweak theory combines the electromagentic and weak force predicting a neutral current, known as the Z^0 bosons, as well as the masses of the Z^0 and $W^\pm$ bosons and the existence of the Higgs boson. Ref. [1]

In 2012, the ATLAS and CMS experiment at CERN confirmed for the first time the measurement of the Higgs boson (H). Ref. [2] It is known to excite a Higgs field giving the particles its mass. Contrary to the gauge bosons, it is a scalar boson with spin 0. It is the heaviest particle detected by now with $\sim 125\text{GeV/c}^2$ (Ref. Fig. 1) and is neutrally charged. Ref. [1]

1.2 Search for New Physics

However, experimental results collected in the last decades show findings that can not be explained in the framework of the SM. Popular examples for unsolved experimental observations are e.g. the uneven matter-antimatter ratio in the universe or the presence of Dark Matter, which seems to interact with matter only through gravity. In a greater context, solutions could be found potentially in theories beyond the standard model. Ref. [3] This search for new fundamental laws in particle physics going beyond the standard model are referred to as New Physics.

The search for new physics has gained popularity with emerging research in the flavour sector, e.g. $b \to cl\nu$ transitions involving the bottom and charm quark (where l refers to the resulting lepton flavour and ν to the corresponding neutrino). Recently, several publications have shown that especially baryonic decays of Λ_b^0, such as $\Lambda_b^0 \to \Lambda_c^+ \mu^- \bar{\nu}_\mu$, are exciting to study with respect to the search of New Physics. Ref. [4–13]

One promising result is a flavour anomaly in B^+ meson decays and concluded to show a potential breaking with Lepton Flavour Universality (LFU). In the SM the leptons differ only by its masses, but not by their interactions. In consequence, the branching fraction of hadrons decaying into electrons or muons should be equal independent of their flavour. Thus, the decays should occur with the same probability. It could be however shown that this is likely not the case in experimental measurements of B^+ mesons at LHCb. If the results are confirmed in future analyses, this finding could point towards NP. Ref. [4] Similar studies using meson decays, involving e.g. K and D mesons, measure directly the coupling of the interaction with respect to the decay flavours. They show as well promising results, which could potentially hint at NP processes. Ref. [13] The coupling constants can however be fitted directly using angular variables. In this analysis the coupling coefficients are expressed by the Wilson coefficients (WC), which will be introduced in the next chapter 1.3. In this analysis, they are directly fitted to the high precision angular data of LHCb in the decay of $\Lambda_b^0 \to \Lambda_c^+ \mu^- \bar{\nu}_\mu$.

Effects of NP in the analysed decay can result in either a variation in the branching fraction or the angular distribution of the decay particles compared to the SM case. To find evidence for NP phenomena two major approaches are used:

1. the direct search for new particles.
2. the high-precision frontier, where NP is searched for indirectly through the effects on SM processes.

This thesis is based on the second strategy in the search for NP in Λ_b^0 baryons.

The standard model decay that is discussed in this thesis is shown in Fig. 2. In the framework of the SM, the Λ_b^0 baryon consists of an up (u), down (d) and bottom (b) quark and the latter decays into a charm quark (c) under the emission of a lepton neutrino pair due to the weak interaction given by the $W^\pm$ boson. The resulting Λ_c^+ baryon then decays into further particles, which are not discussed further. The lepton antineutrino pair in this thesis is a muon (μ^-) - antimuon neutrino ($\bar{\nu}_\mu$) pair. Decays from unpolarised Λ_b^0 are here studied, referring to equally spin-up and spin-down baryons produced and thus the net polarisation being zero, as already studied in Ref. [7, 12].

The resulting antimoun neutrino can not be detected with the apparatus of the LHCb detector. This missing neutrino in the reconstruction arises aberration in the angular distribution, which is analysed in this thesis. Also different spin dynamics of the mediating boson are not completely known today. There are studies predicting a new and heavier spin 1 boson called $W'^\pm$ boson compared to the similar $W^\pm$ boson. This could potentially change the kinematics of the decay, because of a flavour dependent interaction with the leptons. Another idea is the prediction of a new mediator being a charged spin 0 boson H^-, similar to the recently discovered Higgs boson. Ref. [13].

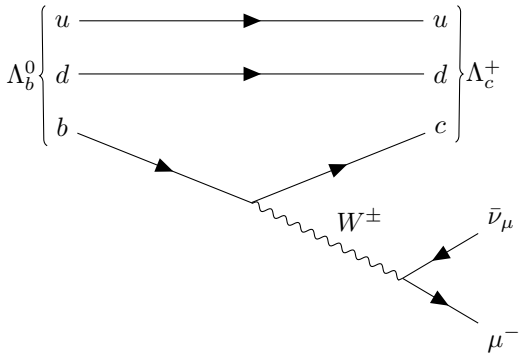

Figure 2: The Standard Model Feynman diagram of the Λ_b^0 decay.

1.3 Wilson Coefficients

Investigating $b \to cl\nu$ transitions the effective Lagrangian introduces the kinematic properties of the decay. The effective Hamiltonian being proportional to its correspondent Lagrangian for this is given by the operator expansion introduced in Eq. 1. Ref. [14] It describes the effective particle interaction in a simplified version, in which the particles do not exchange coupling mediators.

$$H_{eff} = \frac{4G_F}{\sqrt{2}} V_{cb}[(1 + C_{V_L})\mathcal{O}_{C_{V_L}} + C_{V_R}\mathcal{O}_{C_{V_R}} + C_{S_L}\mathcal{O}_{C_{S_L}} + C_{S_R}\mathcal{O}_{C_{S_R}} + C_T\mathcal{O}_{C_T}] + h.c \qquad (1)$$

with G_F the Fermi constant and V_{cb} the Cabibbo-Kobayashi-Maskawa (CKM) matrix element for the $b \to c$ transition, expressing the quark mixing strength in the weak interaction in the SM. The coefficients C_i are referred to as Wilson coefficients, which are set to zero in the SM, but probed to values different from zero in the search for NP. They account qualitatively for short distance interactions in decays and provide the strength to the corresponding operator in the effective Hamiltonian. The $\mathcal{O}_{C_i}$ are the four-fermion operators containing the physics in the NP scenario. The expression in Eq. 1 cancels the heavy particles in decays and shrinks it to a four-fermion operator equation simultaneously keeping all the physics. The operators are either right- or left-handed tensor operators, where $\mathcal{O}_{C_T}$ refers to a left-handed tensor, since the right-handed vanishes as stated in Ref. [15]. In this study no neutrino mixing effects are considered. In the further analysis the Wilson coefficients are referred to as CVR, CVL, CT, CSR and CSL as well as the general short notation WC. By fitting the WCs to model dependent values and reaching a higher precision on their uncertainties, this is a promising goal in the search for NP, which could prove the SM wrong. Therefore, the WCs are the parameters of interest in this thesis. Ref. [14]

1.4 Form Factors

In addition to NP processes, also effects from Quantum Chromodynamics (QCD) need to be accounted for, which follow from hadronic interactions with gluons. These effects are encapsulated in the bi-lepton invariant mass squared q^2 dependent form factors (FF). They are already well known and are in detail introduced for the analysed decay in Ref. [16]. The factors can be varied in multidimensional Gaussian ranges following from Lattice QCD (LQCD) in the toy model fits together with the WCs to receive a better estimate on them as stated in Ref. [5]. They represent a parameter of interest in the further analysis since they are embedded in the differential angular decay density accounting for the angular distribution of the decay products, which is going to be defined in chapter 3.2. Ref. [5, 16].

2 LHCb Experiment

The Large Hadron Collider beauty experiment, LHCb, is located at the Large Hadron Collider Ring (LHC) at CERN in Geneva, Switzerland, togehter with other experiments like ATLAS, ALICE and CMS. Its aim is to investigate heavy flavour physics and to search for evidence of NP in measurements in the decays of beauty and charm quark involving hadrons. LHC reaches center of mass energies of $\sqrt{s} = 14$ TeV (Ref. [17]). With a cross sectional area of $\approx 500\mu$b (Ref. [17]) it is consequently one of the largest $b\bar{b}$ sources worldwide. Therefore, the highest amount of b hadrons, as for example Λ_b^0 can be produced in this experiment. The bottom quark experiment LHCb has a luminosity of $2 \cdot 10^{32}\text{cm}^{-2}\text{s}^{-1}$ (Ref. [17]), being rather small compared to other experiments, however reaching better precision in single pp collisions. In terms of experimental sensitivity, LHCb reaches an integrated luminosity of 9fb^{-1} with 7.5M (Ref. [14]) expected signal candidates of $\Lambda_b^0 \to \Lambda_c^+ \mu^- \bar{\nu}_\mu$ decays. Ref. [17, 18]

2.1 Detector

The detector of the LHCb experiment is a single arm spectrometer covering an angular range in forward direction of 300 mrad in the horizontal and 250 mrad (Ref. [17]) in the vertical plane. Its total extent is about 20m in length and 5m in height (Ref. Fig. 3).

The detector is structured in several subsystems as shown in Fig. 3: first, the beam passes the vertex locator detector (VELO), which measures the track coordinates of the particles near to the location of interaction. Then it reaches the first of the two imaging Cherenkov counter (RICH1), which is together with RICH2 used for particle identification. After this, the beam passes the Tracker Turicensis (TT), such that the detector starts measuring according to the selected requirements. The dipole magnet is located right after the tracking system and measures the momentum of the charged particles. After this, the beam passes several trigger stages and the RICH2 counter. For better particle identification results the beam reaches the electromagnetic calorimeter (ECAL) and the hadronic (HCAL) one, where the energies of the particles can be detected. The last instrument that a beam passes in the spectrometer is the the muon detection system composed by five subsystems and providing information on the resulting muons. Ref. [17]

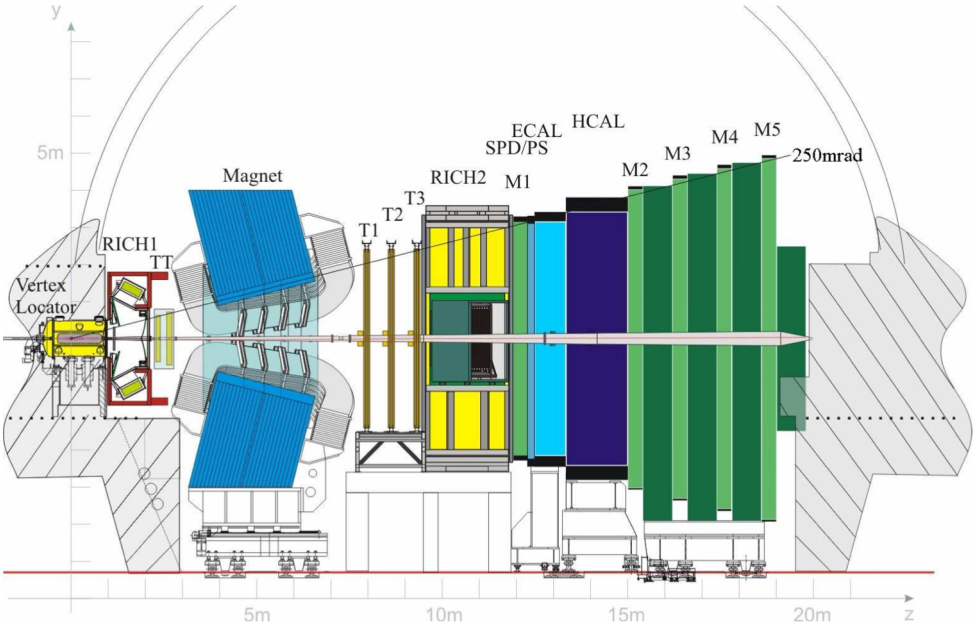

Figure 3: Cross section through the LHCb Detector. Ref. [17]

2.2 Trigger

The Trigger system is mainly composed of front-end electronics fulfilling the requirement of a short latency trigger for fast event selections (L0). In addition, two software (L1, L2) trigger stages

refine the event selection. This was especially designed for complex B meson decays. The first hardware based trigger makes the event selection reducing the number of events of order 1 to 10 and together with the front-end electronics from about 40MHz to maximally 1.1MHz (Ref. [18]). Ref. [17, 18]

2.3 Particle Tracking

To reconstruct the tracks from the particles produced by the proton-proton collisions, several subsystems are needed in the LHCb detector:

1. the VELO.
2. the tracking stations composed by four instruments: the TT located in front of the magnet and the three other trackers (T1-T3) located behind. The latter are divided in an Inner (IT) and Outer (OT) tracking system vertically to the beam pipe.

The reconstruction process of the tracking is shown in Fig. 4.

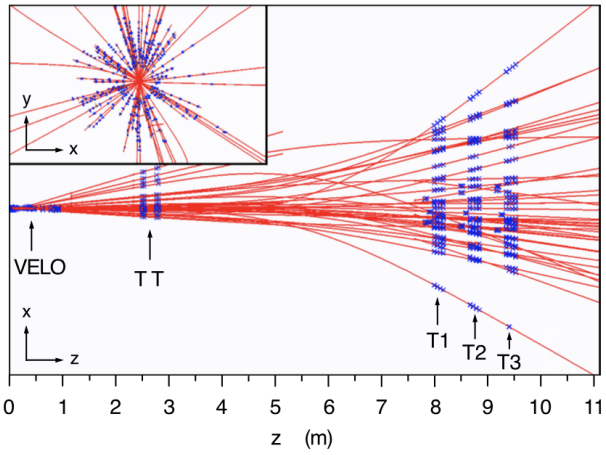

Figure 4: A track reconstruction in the LHCb experiment with the five tracking stages: VELO, TT, T1-T3 in the z-x-plane, respectively in the x-y-plane in the cut-out on the top-left close to the VELO. Ref. [18]

The VELO measures the radial and angular coordinates of the particles along the beam direction. It gives crucial information on the tracks, such that the vertices of the production and decay of the bottom and charm hadrons can be reconstructed. The global performance requirements of the detector include:

- a signal to noise ratio (SNR) greater than 14 (Ref. [17]), which secures an efficient trigger performance.
- an overall channel efficiency, referring to the reduction in noise events in the data set due to a cut selection, of minimum 99% (Ref. [17]) for a SNR being larger than 5.
- the resolution of the spatial cluster of about 4μm at tracks of 100mrad (Ref. [17]) and should not be minimized by irradiation or the sensor design.
- the system needs to be sensitive for particles of a pseudorapidity of $1.6 < \eta < 4.9$ (Ref. [17]) and decaying from vertices in the range of $|z| < 10.6$cm (Ref. [17]) according to the angular acceptance of the detectors the beam passes after the VELO.

Additionally, the VELO is exposed to very high radiation equivalent to 2fb^{-1} (Ref. [17]), which needs to be cooled down and keep the sensors and electronics at temperatures slightly below zero degrees Celsius. Ref. [17]

The TT and the T1-T3 trackers were designed under the so-called name Silicon Tracker (ST) because of their similar properties. Both the TT and the inner part of the T1-T3 consist of silicon

microstrip sensors covering the full acceptance range of LHCb. Each Tracker is structured by four detection layers at which the two middle layers are rotated by a small angle in beam direction. The design of the tracker was chosen according to the following requirements:

- the spatial resolution in single hits using simulations was found to be optimal at 50μm (Ref. [17]) and therefore a total spatial resolution of 200μm (Ref. [17]) was chosen.
- the hit occupancy for the TT (and similar for the IT) defined mainly the geometry of the trackers, which was found to be the highest in the center of the detector and to be reduced at the edges of the tracker. Ref. [17]

Additionally, many other considerations such as the signal shaping time, the single-hit efficiency, the radiation damage, the material budget and the number of readout channels were included for the design of the trackers. Ref. [17, 18]

In contrast to the others, the Outer Tracker (OT) of the LHCb experiment consists of thin straw-tube modules as it is a drift-time detector. Charged particles are measured in location and momentum while passing through the large acceptance area, which requires precise measurements of the invariant mass of the hadrons. The modules are structured in two so-called monolayers of drift tubes filled with a counting gas mixture of Argon and CO_2 to guarantee a short drift time of several nanoseconds. The design was chosen according to the following considerations:

- high rigidity, such that the measurements are not influenced by the tube's position.
- material budget to reduce multiple scattering of particles.

Further, there must be electrical shielding to reduce the noise and the tubes should withstand the enduring radiation. Ref. [17, 18]

2.4 Particle Identification

The identification of the decay results is an important key result of the LHCb experiment. It is especially needed to enable differentiation between pions and kaons in B hadron decays. There exist three different identification stages in the LHCb:

- the two Imaging Cherenkov counters RICH1 and RICH2.
- the calorimeter system consisting of ECAL and HCAL.
- the muon detection instrument.

The Imaging Cherenkov counters are split in two detectors because the detected momentum spectrum is weaker for large polar angles than for low angles and to be able to cover the entire momentum space. RICH1 covers the momentum range from $\sim$ 1GeV/c to 60GeV/c (Ref. [17]) being located between the VELO and the magnet and RICH2 from $\sim$ 15GeV/c to at least 100GeV/c (Ref. [17]) being situated between the Trackers T1-T3 and the first muon detector ring M1. In terms of acceptance coverage, RICH1 covers the range from $\sim \pm$20mrad to $\sim \pm$350mrad horizontally and $\sim \pm$250mrad vertically (Ref. [17]) and RICH2 the range $\sim \pm$15mrad to $\sim \pm$120mrad horizontally and $\pm$100mrad vertically (Ref. [17]), resulting in the full acceptance range of LHCb. The material of the Cherenkov counters need to be adapted for its optimum momentum and acceptance range. Therefore RICH1 consists of aerogel and C_4F_{10} and RICH2 of CF_4. Fig. 5a shows the momentum ranges for the measured Cherenkov angles being dependent on the refractive indices as a property of the gases. Different typical particle momentum ranges are given as well. Ref. [17]

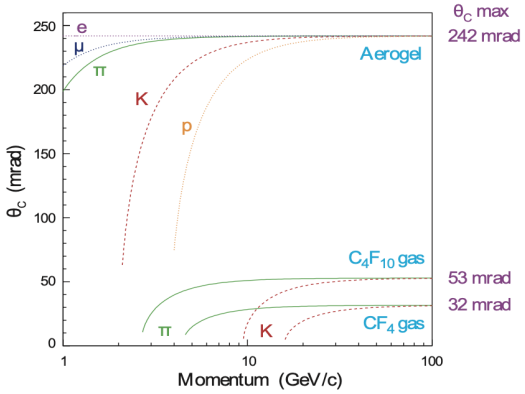

(a) The Cherenkov angle θ_C in dependence of the momenta of the incoming particles and the material in the RICH1 resp. RICH2 instrument.

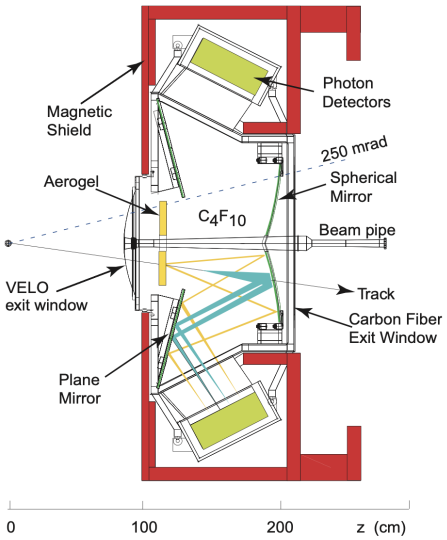

(b) The schematic view of the RICH1 detector showing the mirror system, the photon detectors and the beam pipe location.

Figure 5: The Cherenkov angle dependency on the momentum (left) and the setup of RICH1 (right). Ref. [17]

The detectors use both flat and spherical mirrors to focus the Cherenkov light, at which the optical layout in RICH1 is directed along the beam line and in RICH2 across. The optical system and the instrument layout is shown in Fig. 5b. The detection of the Cherenkov photons in the wavelengths in the range 200-600nm (Ref. [17]) is done using vacuum photon detectors, so-called Hybrid Photon Detectors (HPD). Using them their position and their energy is measured to be able to retrace the particles identity with the known refractive indices of the materials inside the Cherenkov counters. Ref. [17]

Calorimeters are used for particle identification and measurements of position and energy of the detected particles. Simultaneously, they act as a first trigger level by performing a selection on hadrons, electrons and photons. The criterion to pass the selection cut for the electrons is given by high transverse energies and is especially challenging. This ensures that at least 99% (Ref. [17]) of the events of the inelastic proton-proton collisions are filtered from the entire signal spectrum. Beforehand passing the ECAL, a large number of background signals form e.g. charged pion decays need to be rejected, which is done using an electromagnetic shower detection, a so-called pre-shower detector (PS). Even before passing the pre-shower detection the particles hit a scintillator pad detector plane (SPD) to reject a certain amount of neutral pion background signals and select charged particles, e.g. electrons. The principle of the ECAL and HCAL calorimeter is the following: Radiation from the particle decays hit the scintillating material and triggers eventually depending on the energy an avalanche of further particles dissolving from the material, which is also known as a electron resp. hadronic shower. Afterwards, the particles are transported through so-called wavelength-shifting fibres (WLS) to be multiplied and detected by a photo multiplier (PMT) in the end. ECAL's scintillator material is a polymer mixture consisting of polytrene, PTP and POPOP, interacting predominantly through electromagnetic radiation and the HCAL are consisting of iron scintillators interacting with the particles through the strong force. The HCAL consists of two halves build up from in total 52 modules (Ref. [17]) being itself structured again in submodules. This is simpler in construction and designed to be highly uniform and self supporting. The setup of one of the hadronic calorimeter modules is given in Fig. 6. Here, the scintillating plates are arranged alongside with the fibres and are designed with alternating scintillator and absorber material, the latter being laminated steel. Ref. [17]

The last identification instrument in the LHCb experiment is the pentamerous Muon detector. Muons are often decay products of heavy B decays, as well as in the Λ_b^0 decay studied in this thesis and are therefore important to analyse in the frame of New Physics. Each detector measures the space points of the tracks, giving a binary signal to the trigger system, which includes a separate

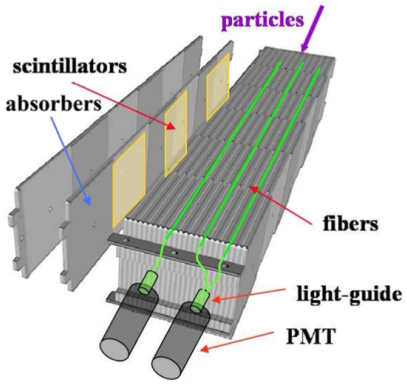

Figure 6: The schematic view of the HCAL Calorimeter Module with the WLS fibres, the PMT Photomultipliers, and the detailed view of the alternating scintillator and absorbers structure. Ref. [17]

muon track reconstruction system, selecting only for events triggered in all five detectors. The stations M2-M5 are placed after the HCAL instrument and the M1 beforehand. The angular acceptance of the different stages are from 20 to 306mrad (Ref. [17]) in the horizontal instrument axis and slightly less in the vertical axis. The detectors become larger with the distance to the collision point because the angular acceptance range becomes larger as well. In terms of spatial resolution, M1 to M3 have a higher resolution compared to M4 and M5, since the first detectors need to define the track of the particle in better detail than the last ones. The regions of angular detection called R1-R4 increase parallel to the beam line. Between the detectors, there are iron absorbers implemented for moun selection. Ref. [17]

The detectors consist of Multi-Wire Proportional Chambers (MWPC), except the inner part on M1 being a more radiation enduring detector called GEM. MWPC show a complex chamber structure filled with a gas mixture, giving an electrical signal if a particle is detected. All five detectors must return a positive signal, such that the trigger detects the event. Ref. [17]

In the next chapter, the underlying principles for the data analysis in this thesis of the data sets received by the LHCb detector are introduced.

3 Analysis Framework

To improve the estimation and to find potential systematic uncertainty sources on the Wilson coefficients using toy models, two aspects are considered for improvement:

1. Different binning schemes on the phase space can lead to a bias on the estimation of the Wilson coefficients. The binning study investigates this effect. This will be structured in a sensitivity analysis to detect on which region of the phase space the fits are most sensitive to, followed by the choice of the binning schemes and concluded with the comparison of the degradation of the WC values for each binning scheme in contrast to an optimal scheme.

2. The fits on the Wilson coefficients are model dependent, such that the wrong choice of the efficiency and resolution in the model could produce systematic uncertainties. These uncertainties are studied in the model dependency analysis. This begins with the definition of variation scenarios and model variation cases, followed by the definition of the probability distribution function weights acting as the basis for the fits. The analysis is concluded with the discussion of the difference in true and reconstructed values for various scenarios.

As a basis for the binning and model dependency analysis the following concepts and definitions need to be introduced.

3.1 Phase Space

The phase space describes the space of the dynamical variables resulting in all the different possible states of a system and its dimensions define the degrees of freedom of the data. Since in this analysis only the decays of unpolarised Λ_b^0 are studied, the phase space is a bi-dimensional system defined by the following variables:

- q^2: the four-momentum transfer of the muon - antimoun neutrino in the decay, which is a measure of the transferred energy. In this study, it is given in units of $[\mathrm{GeV}^2/\mathrm{c}^2]$.
- $\cos\theta_\mu$: the angular deflection of the generated muon, which is dependent on the differential decay density.

The datasets retrieved from the decay density as well as the toy model, introduced in 3.2 and 3.3.1, consist of data points being described by two dimensional vectors:

$$\vec{x} = [q^2, \cos\theta_\mu] \tag{2}$$

For polarised Λ_b^0 decays there are additional four phase space variables to be accounted for, which are not further discussed. Ref. [14]

3.2 Differential Decay Density

The differential decay density gives the angular distribution of the decay products in dependence of the phase space parameter q^2 and $\cos\theta_\mu$. To be able to qualitatively understand the NP contribution to the decay in the angular distribution, the decay density is the crucial variable as it is compared to the SM case. It is retrieved for this decay by integrating the six-fold normalised angular differential decay density over all phase space variables except for q^2 and $\cos\theta_\mu$. The density is given in Eq. 3. Ref. [14]

$$\begin{aligned}\frac{d^2\Gamma}{dq^2 d\cos\theta_\mu} = \frac{N}{\Gamma}\Bigg[2\pi^2\Bigg[\cos\theta_\mu\Bigg(&-2\cos\theta_\mu(|I_7|^2+|I_8|^2) + 2I_6^*(\cos(\theta_\mu I_6 + I_{10}) - \cos(\theta_\mu)I_2 I_2^* + \\ &(\cos\theta_\mu - 2)I_3 I_3^* + (\cos\theta_\mu + 2)I_4 I_4^* + 2I_5^*(\cos\theta_\mu I_5 + I_9)\Bigg) + |I_2|^2 + |I_3|^2 + |I_4|^2 + \\ &I_1^*(I_1 - \cos\theta_\mu{}^2 I_1) + 2I_{10}^*(\cos\theta_\mu I_6 + I_{10}) + 2I_9^*(\cos\theta_\mu I_5 + I_9) + 2I_7 I_7^* + 2I_8 I_8^*\Bigg]\Bigg]\end{aligned} \tag{3}$$

The terms I_i include the Wilson coefficients to the differential decay density. They depend further on the form factors, which themselves are functions of q^2. The exact formulations can be found

in Ref. [14]. The I_i for $i = \{1, 2, 3, 4\}$ are functions of $C_{V_L}, C_{V_R}, C_T, a_l, b_l, b_T, c_A, c_V$ and c_T. For $i = \{5, 6, 7, 8\}$ the terms are expressed in terms of $C_{V_L}, C_{V_R}, C_T, a_l, a_T, b_A, b_l, b_V$ and d_T and for $i = \{9, 10\}$ on $C_{V_L}, C_{V_R}, C_{S_L}, C_{S_R}, a_l, a_A, a_P, a_S, a_V$ and b_l. The coefficients a_V, a_A, b_V, b_A, c_V and c_A depend explicitly on q^2 and similar as a_S and a_P can be expressed using the form factors $F_{0,+,\perp}$ and $G_{0,+,\perp}$. These form factors are also present in the SM. The coefficients a_T, b_T, c_T and d_T are defined in dependencies of the tensor form factors $h_+, h_\perp, \tilde{h}_+$ and $\tilde{h}_+$, which need to be accounted for in NP scenarios. Ref. [14]

3.3 Monte Carlo simulations

Using Monte Carlo (MC) simulations many target events can be generated using a model, which results in a reconstructed data set. There are two main classes of Monte Carlo simulations: The first method is referred to as *toy models*, being defined by a specific simplified model and can be used to estimate the effect of given assumptions on the resulting observable. This is achieved using a fitting procedure, e.g. the fitting parameter being the Wilson coefficients or the form factors. The second method is the *full simulation*. It is used for the generation of events for different variables in the phase space resulting in a reconstructed data set. This simulation is extremely delicate and has each component of the detector encoded very precisely, such that the data set resembles a natural distribution of events in highest precision. The Monte Carlo method here employed is based on an 'accept/reject' strategy in order to distinguish values fulfilling the chosen selection criterion.

3.3.1 Toy Models

In this thesis, toy models were used to fit for WC and FF. The underlying probability density function defining the model in this analysis is given by Eq. 4.

$$PDF(\vec{x}_R, \vec{\theta}) = \frac{1}{N} \int R(\vec{x}_R, \vec{x}_T)\epsilon(\vec{x}_T) f(\vec{x}_T; \vec{\theta}) d\vec{x}_T \tag{4}$$

with $\vec{x}_R = (q_R^2, \cos\theta_R)$ being the reconstructed phase space values; $\vec{x}_T = (q_T^2, \cos\theta_T)$ being the true phase space values; $\vec{\theta}$ the fit variables including WC and FF; $f(\vec{x}_T; \vec{\theta})$ the physics containing dynamic function; N being the integral normalisation; $R(\vec{x}_R, \vec{x}_T)$ the *resolution* function on the reconstructed phase space variables accounting for bin migration during the fits. Due to the missing neutrino information in the decay, as it was introduced in chapter 1, the phase space variables are not entirely known and the model fits need to be binned. This leads to the bin migration which needs to be corrected for with the help of the response matrix being. $\epsilon(\vec{x}_T)$ refers to the *efficiency* of the true variable giving the probability of an event passing certain selection requirements. The fitted values of the WC depend on these criteria and therefore are a potential source of systematic uncertainties, which need to be analysed.

Since in this analysis the fits are binned, we use the following slightly varied expression of Eq. 4 in a discrete form, shown in Eq. 5.

$$PDF(\vec{x}_R^i, \vec{\theta}) = \frac{1}{N} \sum_{i,j} R(\vec{x}_R^i, \vec{x}_T^j)\epsilon(\vec{x}_T^j) F(\vec{x}_T^j; \vec{\theta}) \tag{5}$$

where $F(\vec{x}_T^j; \vec{\theta})$ is the primitive function of the dynamic function f evaluated in the j-th bin. The efficiency and resolution are considered to be uniform throughout each bin. In the first part of the analysis the efficiency and resolution factors will be neglected, setting the values to one. In the second part, the change in resolution and efficiency depending on the given reconstructed and fitted values are investigated. Due to the dependency of the model on the reconstructed values this study is also referred to as *model dependency analysis*.

4 Binning Scheme Analysis

Until now in the $\Lambda_b^0 \to \Lambda_c^+ \mu^- \bar{\nu}_\mu$ angular analysis a regular binning scheme of 5x5 = 25 bins has been adopted. To improve the performance of the fits on the WCs, another binning scheme could be chosen to improve the sensitivity of the fit to the WC and the corresponding systematic uncertainty. This analysis will focus mainly on the Wilson coefficient CVR due to high sensitivity to the fits. The analysis was performed as well on the other coefficients to extend the understanding of the WCs. It uses results from fits to the phase space variables, which leads to the PDF shown in Eq. 5 with fixed form factors values to the Lattice QCD estimate. Ref. [14] For this analysis, the efficiency and resolution in the model are supposed to be unitary.

4.1 Sensitivity Analysis

To understand where the sensitivity of the Wilson coefficients to the fit is the highest in the phase space and thus to refine the binning scheme in appropriate regions, a sensitivity analysis was performed. The sensitivity is computed as the difference between the fitted probability distribution and the expected standard model distribution. The WCs were sampled 100 times in uniform distributions with its ranges given in the appendix in the appendix and given from Ref. [5]. To compare the largest variations, the maximum of the differences was taken.

$$\Delta = \max\{\mathrm{PDF}_{\mathrm{NP}} - \mathrm{PDF}_{\mathrm{SM}}\} \tag{6}$$

where Δ is the maximum sensitivity in 100 samples, $\mathrm{PDF}_{\mathrm{NP}}$ the fitted WC distribution in the phase space and $\mathrm{PDF}_{\mathrm{SM}}$ the standard model distribution with all WC set to zero.

The sensitivity to the WC obtained from the study is shown in a regular 60x60 binning scheme Fig. 12. CVR and CT seem similar with high sensitivity in the high q^2 and low $\cos\theta$ region. CSR and CSL however show high sensitivity in regions of low $\cos\theta$ and only small sensitivity for $\cos\theta$ being zero.

Comparing the maximum absolute sensitivity of the different WCs, CVR shows the largest sensitivity, then CT and CSR follow and CSL shows the least absolute variation, which is consistent with the results from Ref. [16].

$$\Delta_{CVR} > \Delta_{CT} > \Delta_{CSR} > \Delta_{CSL} \tag{7}$$

Since the current fitting regime is most sensitive to CVR, this coefficient is especially interesting in the search for New Physics and the main coefficient of interest in this study.

The fit is not sensitive to the coefficient CVL, which is in agreement to the results presented in Ref. [16]. Therefore the variability is simply randomly distributed over the phase space, as shown in Fig. 13.

4.2 Selection of Binning Schemes

In this study, seven different binning schemes were selected with a different number of bins and either equidistant bin edges, corresponding to a regular scheme, or manually chosen bin edges, corresponding to an irregular binning. While choosing the bins manually, special emphasis was put into the regions with high variability of CVR. These regions were binned more densely than regions with low variability. Later in this analysis on each of the bins a fit was performed, therefore the maximum number of bins was decided to be $n \leq 45$. Binning 0 was decided to be the worst case binning scheme having as many bins as degrees of freedom in the fits, so $n = 12$. The best case scenario and control binning scheme was chosen to be binning scheme 6 with a total of $n = 1600$ bins. The chosen binning schemes are composed in table 1 and given explicitly in the appendix.

To be able to evaluate which binning scheme could potentially reduce uncertainties a comparison to the control binning scheme 6 was conducted. This included performing fits on each bin separately using a Monte Carlo toy model with 75 Mio. data samples. On each binning, 500 data samples using different seeds to estimate the statistical variation of the toy models were generated. The non-normalized mean and standard deviation of the $\mathrm{PDF}_{\mathrm{Fit}} - \mathrm{PDF}_{\mathrm{SM}}$ distribution are the parameters of interest, where $\mathrm{PDF}_{\mathrm{Fit}}$ corresponds to the resulting probability distribution from the fit and $\mathrm{PDF}_{\mathrm{SM}}$ to the probability distribution were the WCs are set to zero. The parameter of interest are later compared to the control scheme of 40x40 bins and were found using a Gaussian fit in

Table 1: The selected binning schemes and their regularity with Scheme 6 being the control binning.

Binning Scheme	Number of Bins (Columns x Rows)	Regularity
0	4x3	Regular
1	6x4	Irregular
2	5x5	Regular
3	7x5	Irregular
4	7x5	Regular
5	7x6	Irregular
6	40x40	Regular

Python using the function *scipy.optimize.curve_fit*. The error on the mean σ_{mean} and standard deviation σ_{stddev} was given by the standard error of the distribution σ with n the number of fits (in this study $n = 500$):

$$\sigma_{mean} = \frac{\sigma}{\sqrt{n}} \qquad \sigma_{stddev} = \frac{\sigma}{\sqrt{2n-2}} \tag{8}$$

4.3 Binning Scheme Comparison

To compare quantitatively the binning scheme improvement to the control binning scheme 6 for the different WCs the degradation in percentage was calculated by Eq. 9 and plotted in Fig. 10. The results for the degradation of all binning schemes are composed in table 4 in the appendix. The less the absolute degradation in comparison to the control scheme, the better the scheme resembles a continuous phase space respectively an unbinned case, which is desirable. In consequence, the degradation is a measure for the systematic uncertainty on the WCs due to the chosen binning scheme.

$$D = \left(1 - \frac{\sigma_i}{\sigma_6}\right) \cdot 100 \tag{9}$$

where D is the degradation and σ_i the standard deviation on the i-th binning scheme.

The following figures show the results of the binning analysis in the case for CVR, whereas the figures for the other WCs can be found in the appendix. In Fig. 7 the binning scheme dependent distributions of the 500 fits for the CVR are presented. They include the Gaussian fit on the distribution, resulting in the mean and standard deviation estimates, which is used later in the analysis.

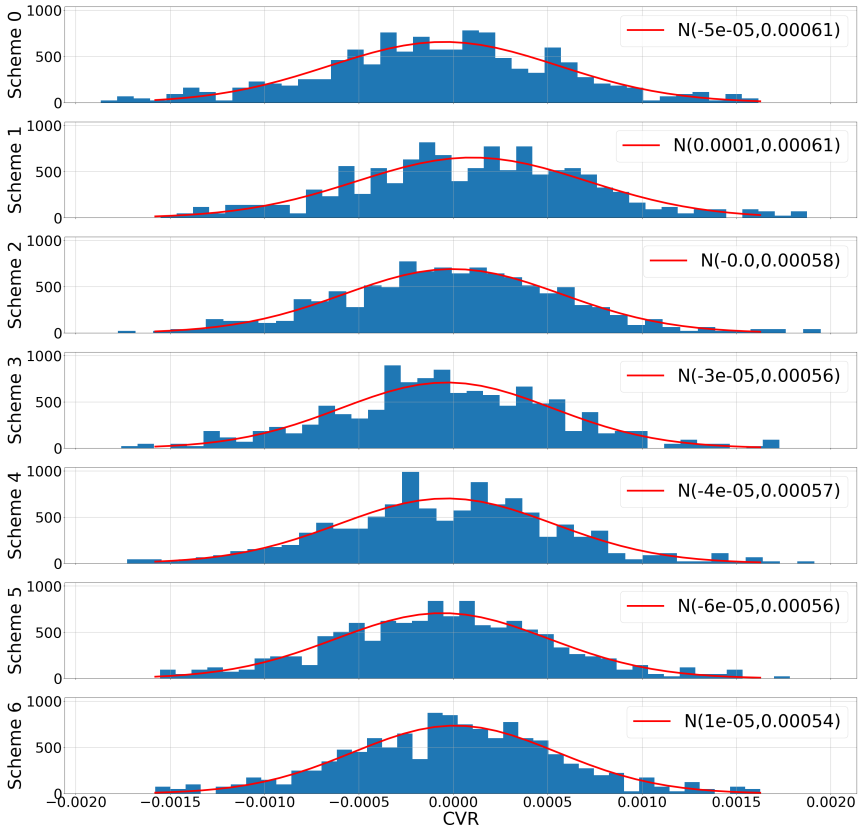

Figure 7: The CVR value distributions and the Gaussian fit for different binning schemes.

The fitted mean values and their standard deviation of CVR are given in Fig. 8 with the uncertainty shown in the brackets representing the probability that this value lies within the error on the mean range, calculated by the mean divided by the standard deviation. One sigma corresponds consequently to 68%.

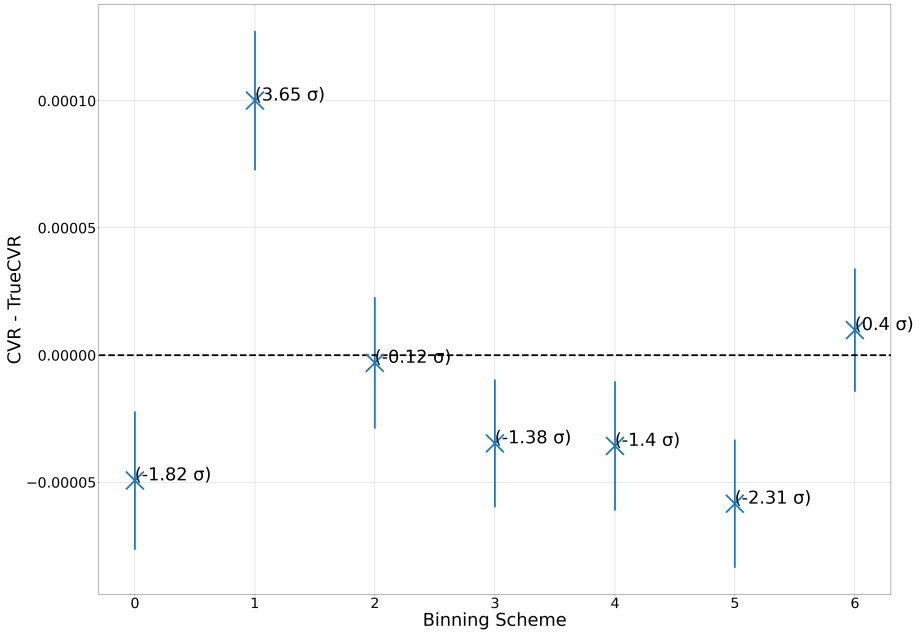

Figure 8: The CVR mean and fitted standard deviation.

The fitted standard deviation of each binning for CVR is given in Fig. 9. Here, binning scheme 3 and 5 show the smallest standard deviation and therefore a small systematic uncertainty on the WC coefficient.

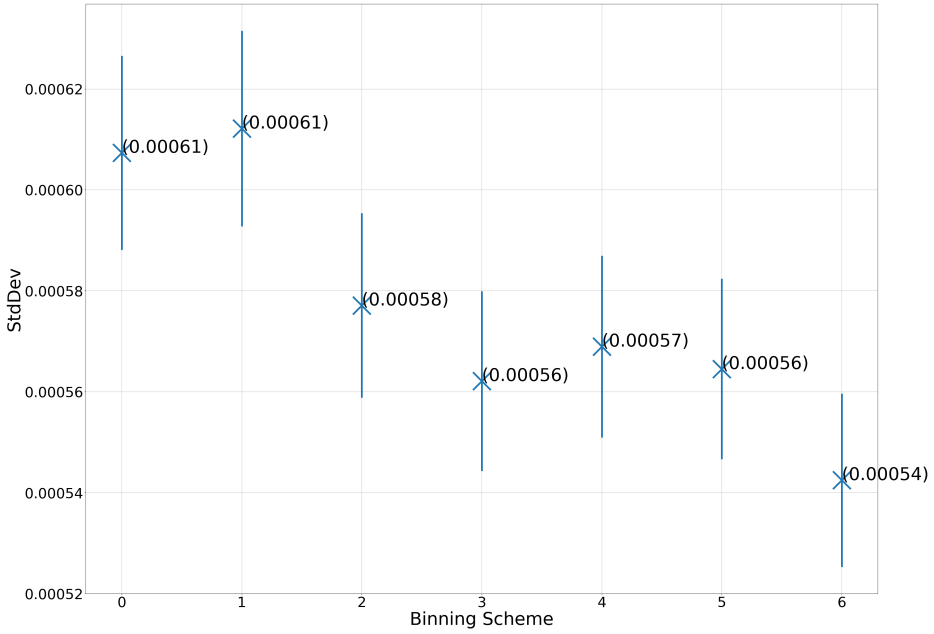

Figure 9: The CVR fitted standard deviation.

The main result of the binning analysis is the degradation in terms of the chosen scheme and WC, which is presented in Fig. 10.

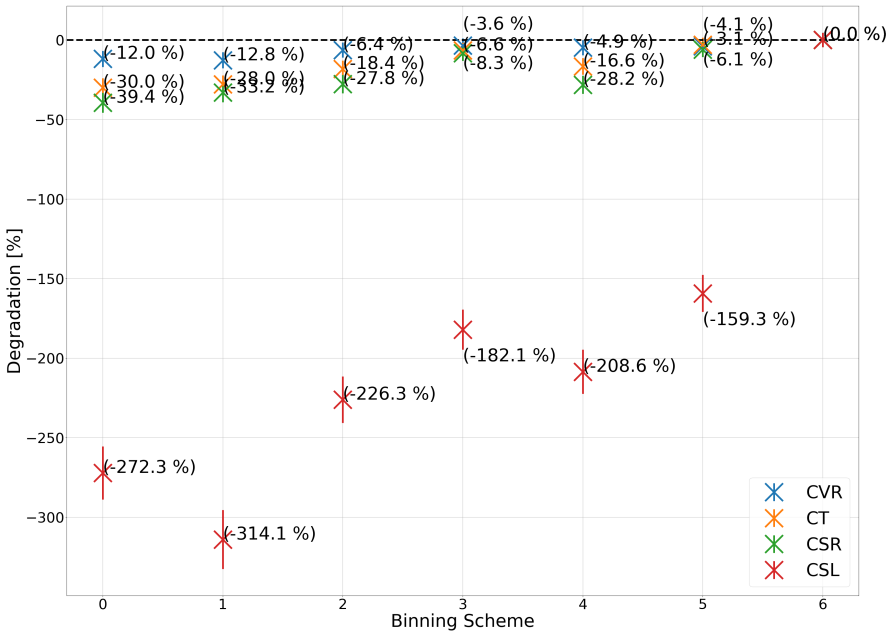

Figure 10: The degradation of the Standard deviation on the WC value distribution in dependence of the binning schemes with respect to the control binning scheme 6 with no FF being floated.

Compared to the *original binning scheme*, corresponding to *binning scheme 2*, a decrease of the systematic uncertainty on the WCs due to the binning scheme can be reported. By analysing the degradation plot, schemes 3 and 5 show the least absolute degradation. For CVR, scheme 3 shows even less absolute degradation compared to scheme 5, in contrast to the other WCs. CSL shows a very high degradation in each binning scheme, however becoming slightly less for schemes 3 and 5. This arises from the fact that the schemes were chosen according to the variability in CVR, which looks different for CSL as seen in Fig. 12. Additionally, the fact that scheme 3 and 5 are chosen to be an irregular binning, show less absolute degradation in the comparison to the similar regular schemes 2 and 4. Comparing scheme 4 (Regular 7x5) to scheme 5 (Irregular 7x6), a clear decrease in absolute degradation is visible. Scheme 5 reduces the absolute degradation and with that the systematic uncertainty relative to the original scheme 2 by 2.3% for CVR and even more for the other WCs, what follows from table 2.

Table 2: The degradation in dependence of the binning schemes 2 and 5 for CVR, CT, CSR and CSL.

Deg	Scheme 2	Scheme 5
CVR	-6.4 ± 4.8	-4.1 ± 4.7
CT	-18.4 ± 5.3	-3.1 ± 4.6
CSR	-27.8 ± 5.7	-6.1 ± 4.8
CSL	-226.3 ± 14.6	-159.3 ± 11.6

Further, the original scheme is a 5x5 regular binning, corresponding to 25 bins and consequently accounting for 25 fits per data sample. Therefore, an improvement on the scheme with an adequate increase in the number of bins is desirable. With binning scheme 3 there would be an increase of $|35 - 25| = 10$ bins, so by 40% and with scheme 5, $|42 - 25| = 17$ bins, so by 68%. However, since the degradation is the most important parameter and an increase in bin number of 68% is

acceptable, binning scheme 5 is chosen as the optimum.

Additionally, from table 4 it can be concluded that binning scheme 0 (Regular 4x3), which corresponds to the worst case scenario, shows a higher degradation compared to the original binning scheme 2, as it was expected from the number of bins introduced in the chapter 4.2.

In conclusion, *binning scheme 5* - an irregular 7x6 scheme - is the preferred scheme to be used from now on in the study.

5 Model Dependency Analysis

In this part of the analysis, a model dependency study was conducted. To reduce background contributions in data, selection cuts depending on discriminating observables are applied. However, in practice these observables are always slightly correlated to the fit variables leading to non-uniform selection of Λ_b decays across the phase space. Therefore, the theoretical PDF or phase space distribution needs to be adapted and the phase space variables can not simply be fitted using this PDF. To be able to quantify the effect of selection cuts and reconstruction, Full Monte Carlo simulations are used as introduced in Chapter 3. By using them, the probability of an event passing the selection cuts or not as a function of q^2 and $\cos(\theta)$ can be estimated. The resulting probability distribution is also called *efficiency map*, since it corresponds to a four dimensional matrix depending on the phase space variables of the true and reconstructed model: $[\vec{x}_{rec}, \vec{x}_{true}]$.
Another reason for systematic uncertainties on the fit model is the decrease in resolution on the phase space due to the unreconstructed neutrino in the Λ_b^0 decay. Also reconstruction effects in the detector lead to a Gaussian distributed smearing of the signal with the corresponding sigma being the experimental resolution. Due to the binning this consequently results in bin migration. This effect needs to be accounted for in terms of a response matrix being a four dimensional, phase space dependent matrix. Since the simulations are based themselves on theoretical decay models, a systematic uncertainty must be included, for which the model and the resulting efficiency and response maps must be corrected in further studies. Ref. [14]

The procedure of the analysis is the following: in a first step, a SM refence data set is generated with the FF fixed to LQCD central values and the WC set to zero giving the SM truth distribution. The next step is to fit this data set in different scenarios to one of the WCs or the FFs, corresponding of the estimated parameter in the fit. The SM reference data set is fitted with different model scenarios, which are introduced in the next chapter. After this, the resulting data set is fitted again to the fit scenarios with the same SM toy model. Using the standard deviation and the mean on the distribution of the 100 samples the systematic uncertainty on the model can be estimated.

5.1 Scenario Definition

In the following part of the analysis several model scenarios are defined, which are combined in the following table 3. In the model scenario, the efficiency and/or the resolution have been varied, such that the model has been varied.

Table 3: The five model scenarios with either the FFs or the WCs varied.

	WC	FF
SM	set to 0	varied
CVR	varied	fixed
CT	varied	fixed
CSR	varied	fixed
CSL	varied	fixed

In the fixed FF cases, the form factors are set to central LQCD values, which are introduced in Ref. [16]. If they are varied, they are sampled randomly from a multidimensional Gaussian PDF, arising from LQCD as introduced in Ref. [16]. The WCs are varied in the Gaussian distributions given with the mean zero and a standard deviation set to the maximum value of the uniform distribution given in the appendix.

For each of the model scenarios there were three different cases defined corresponding to the model variation in either efficiency or resolution:

- Case 1: Efficiency varied, Resolution fixed
- Case 2: Efficiency fixed, Resolution varied
- Case 3: Efficiency varied, Resolution varied

Each model scenario was sampled 100 times, in each of the three configurations and for each of the five fit scenarios (corresponding to either FF, CVR, CT, CSR or CSL varied). The above introduced procedure gives for each model and fit scenario, each model variation and each sample in total a data set of 5x5x3x100 = 7'500 fit results, which will be used for the model dependent scenario in chapter 5.3.

5.2 Weight Definition

To define the input of the efficiency and resolution maps the weights were extracted from the MC toy model using randomized WC or FF values. The WCs were sampled in a Gaussian distribution with the mean set to zero and the standard deviation chosen to be the maximum value of the edges of the uniform distribution, which is given in the appendix. The FF were retrieved all together from a multidimensional Gaussian probability density function (PDF) with its mean and standard deviation following from LQCD. The weight is defined in Eq. 10:

$$\mathrm{PDF}_{\mathrm{weight}} = \frac{\mathrm{PDF}_{\mathrm{new}}}{\mathrm{PDF}_{\mathrm{old}}} \tag{10}$$

with $\mathrm{PDF}_{\mathrm{old}}$ being the probability density function with fixed WCs and FFs and $\mathrm{PDF}_{\mathrm{new}}$ the function with the varied parameters inside the above mentioned distributions. For each of the model scenarios introduced above and for each of the 100 samples a weight was defined. Later, using the weights the fits on the fit scenarios were performed.

5.3 Model Dependent Scenario Comparison

From the fit results an estimate of the systematic uncertainty on the model can be reported. The difference: $\mathrm{WC}_{\mathrm{true}} - \mathrm{WC}_{\mathrm{reconstructed}}$ is displayed, where the true value corresponds to the efficiency and resolution set to fixed SM values and the reconstructed to the one being modified due to weights in the toy model, as it was introduced in Eq. 5 and chapter 5.2.

In a first step, the model dependency on the WC was discussed by comparing the fit results of the model scenario being equal to the fit scenario for each WC. The results are given in Fig. 18, where the distribution for 100 samples of the variation in WC on the model is plotted. The model dependency is split in the three variation cases either the efficiency or the resolution or both being varied. Comparing the model variation cases, the standard deviation on the efficiency and resolution are of the same order and thus have both a similar impact on the WC values. The bias due to the selection requirements account for the same systematic uncertainty as for the bin migration. Also, it is important to mention that the systematic uncertainty is the smallest for CVR and with a standard deviation of 0.0009 it is comparable to the statistical uncertainty for one sigma of 0.001 in the $pK^-\pi^+$ case, as it is stated in Ref. [14]. This is favourable for the analysis meaning that the above introduced procedure to retrieve the CVR values raises an adequate bias on its value.

In a second study, similarly as before, the systematic uncertainty on the FFs due to variations in the SM model scenario are discussed. So the fit and model scenario correspond to the SM case, setting the WCs equal to zero, but varying the FFs. Here, for all FFs a Gaussian distribution is received depending on the efficiency or resolution varied, as it is displayed in Fig. 19. The variation on the resolution has a larger influence on the FF value variation than the efficiency. This is as well, a positive result, showing that the selection requirements were chosen adequately and that mainly the bin migration must be accounted for. Since the distribution in the 'both varied' case has a strong tendency to be larger than each of the cases itself, the correlation between the efficiency and resolution bias is supposed to be positive.

To improve the understanding of the influence of the model variation on the fitted values of the WCs, a third and crucial study was conducted. The WC distributions on the fit scenarios are plotted for the three model variation cases, as it is shown by Fig. 11.

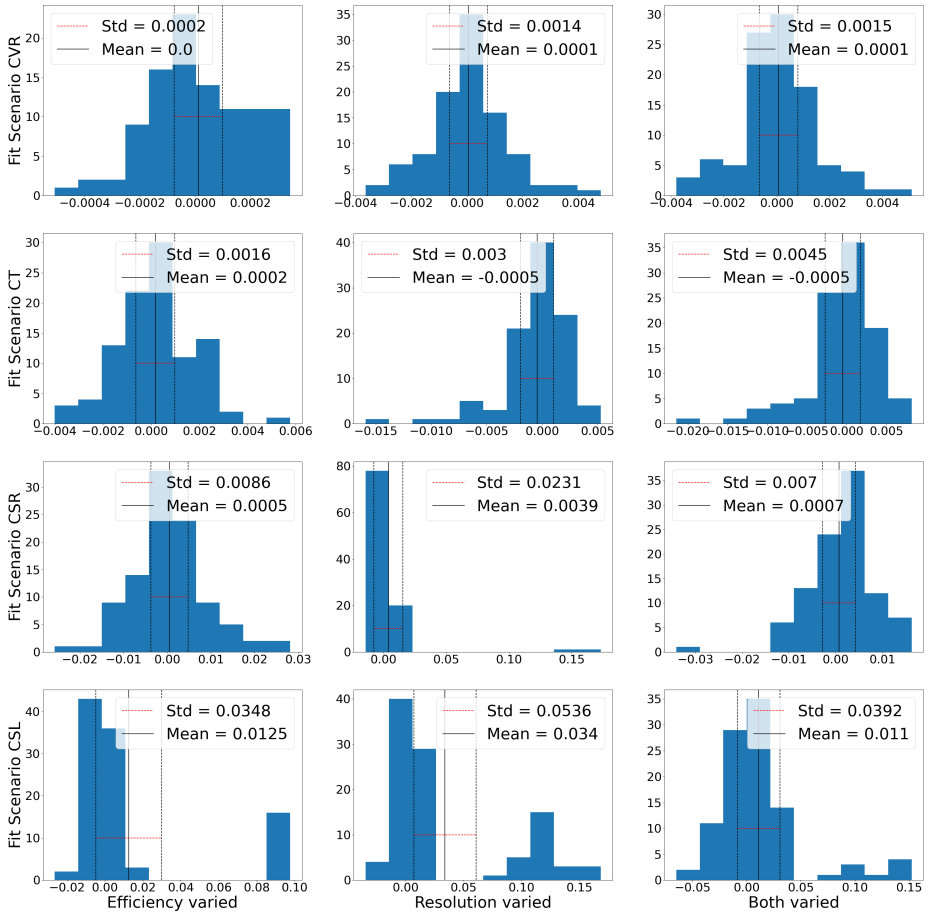

Figure 11: The WC value distributions depending on the model variations with the model scenario set to SM and the fit scenario set to each WC showing the influence of the model variation in the standard model case on the fitted WC values.

The model scenario was chosen to be a SM scenario with only the FFs varied and the fit scenario was set to each WC separately. The distribution follows a Gaussian distribution due to the sampling regime. For CSR and CSL a small second peak is visible emerging from a second order local extrema in the fit, where the fit eventually converges to. This study concludes a value for CVR with both model variation taken into account of around 0.0001 ± 0.0015. This corresponds to an around three times larger overall systematic uncertainty compared to the same value in the first study, where the fit and model scenario were set both to WC values. If both model variations are taken into account, the systematic uncertainties tend to be larger than the two variations added separately in square, such that the correlation in this case seems to be negative. The model variations are mostly larger for the case were only the resolution is varied compared to the efficiency variation. In the case for CVR, this is especially distinct with a standard deviation due to resolution of 0.0002 and due to the efficiency of 0.0014.

Thus, the systematic uncertainty of the model variation on the WC fits is small, but not neglectable and mainly due to a bias in resolution.

Conclusion

The search for New Physics has become more and more exciting during the past years. One aspect here is to aim for the aberration in angular distributions of modelled data compared to measured data. To refine the fit estimates on (partially) unknown parameters, as it was discussed for the WCs and FFs in this study, sources of systematic uncertainties need to be diminished. In this thesis two particular aspects have been analysed.

In the binning scheme analysis an optimal binning scheme has been evaluated, consisting of an irregular 7x6 binning scheme, which improves the systematic uncertainty on the binning scheme for CVR by 2.3% compared to the before adapted scheme.

The result of the model dependency analysis shows that the fits of WC and FF are slightly biased due to model variations. The resolution variation here has generally a larger effect on the bias of the WC values than the variation in the efficiency.

In a further study, the efficiency and resolution maps need to be corrected for this bias by e.g. an iterative approach on the fit. This would reduce the bias on the WC and FF fits in order to estimate their values with higher precision. If the WC as well as the FF are better known, the aberration compared to the SM can be described in more detail and potentially disprove or expand today's known theories. Furthermore, there are other parts of the model that need to be improved, such as the corrected mass fit, accounting for effects on the signal yield determination, which have been neglected in this study.

More and more research is done in the field of New Physics reaching higher precision on the estimates of nonzero observables, like the Wilson coefficients, potentially resulting in new descriptions of the today's known theories. In the future, this may solve some of the most fundamental questions in modern particle physics.

Acknowledgements

I want to thank my supervisors for their exceptional support during the entire process of the thesis. I want to express my gratitude to the Physics Department and the entire LHCb group at the University of Zurich supervised by Prof. Nicola Serra for letting me add a contribution to the analysis of LHCb data. Certainly, I want to thank Dr. Patrick Owen for guiding me through the process of this thesis and for giving me the opportunity to work on a highly interesting topic that pushes the boundaries of currently known foundations in physics. I highly appreciated the meetings with Dr. Abhijit Mathad as well as his readiness to answer my questions at all times, which was extremely helpful and crucial for me to understand in better detail the complex topic and the analysis on the data. Furthermore, I am very grateful for the discussions with Martina Ferrillo during the meetings as well as her generous and valuable support to improve my thesis. Concluding, I highly appreciated the weekly meetings and the aspiring discussions about the findings and further analysis. I am very excited where this cutting-edge field of particle physics will lead with the help of future analyses.

Appendix

Binning Scheme Analysis

The WC were varied in the following uniform distribution ranges using the *numpy.random.uniform* function with 100 samples from Ref. [5].

- CVR: uniform($[-0.020, 0.030]$)
- CT: uniform($[-0.050, 0.050]$)
- CSR: uniform($[-0.460, 0.306]$)
- CSL: uniform($[-0.490, 0.350]$)
- CVL: uniform($[-0.044, 0.020]$)

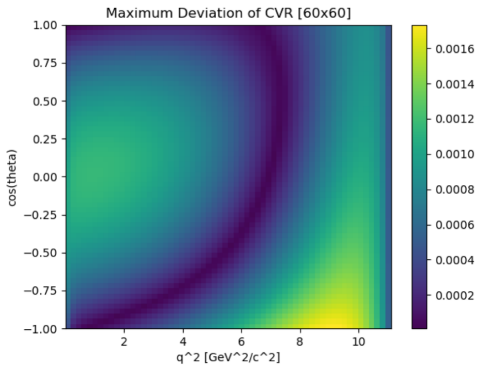

(a) CVR sensitivity.

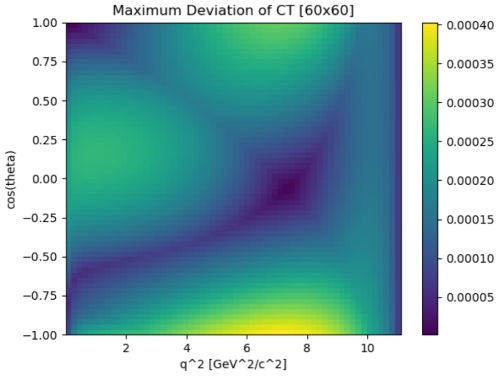

(b) CT sensitivity.

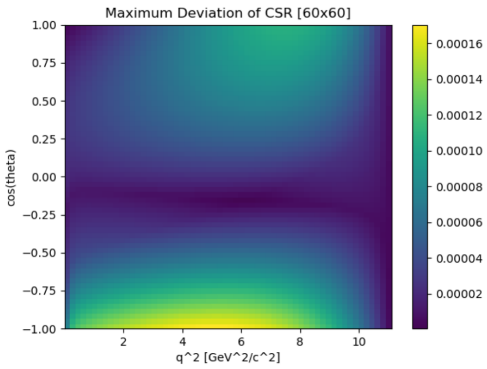

(c) CSR sensitivity.

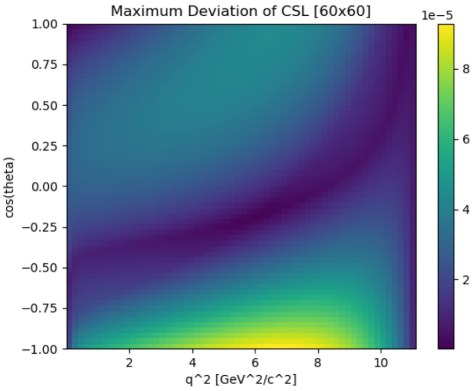

(d) CSL sensitivity.

Figure 12: The maximum sensitivity of CVR (top-left), CT (top-right), CSR (bottom-left) and CSL (bottom-right) in a 60x60 scheme as introduced in 4.1.

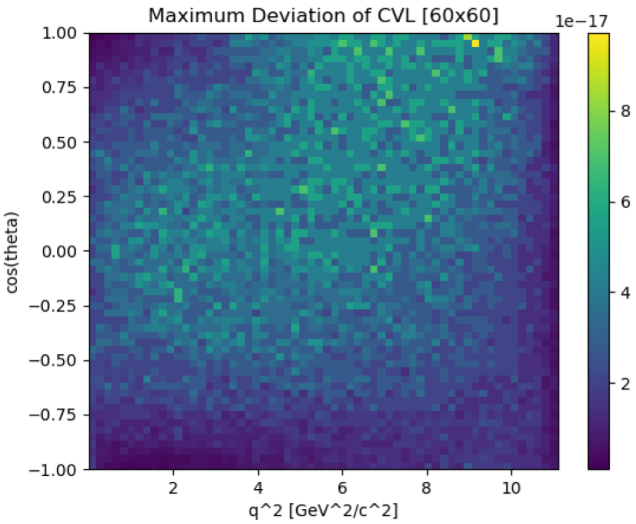

Figure 13: The maximum sensitivity of CVL in a 60x60 scheme showing a pure random fluctuation as expected as described in 4.1

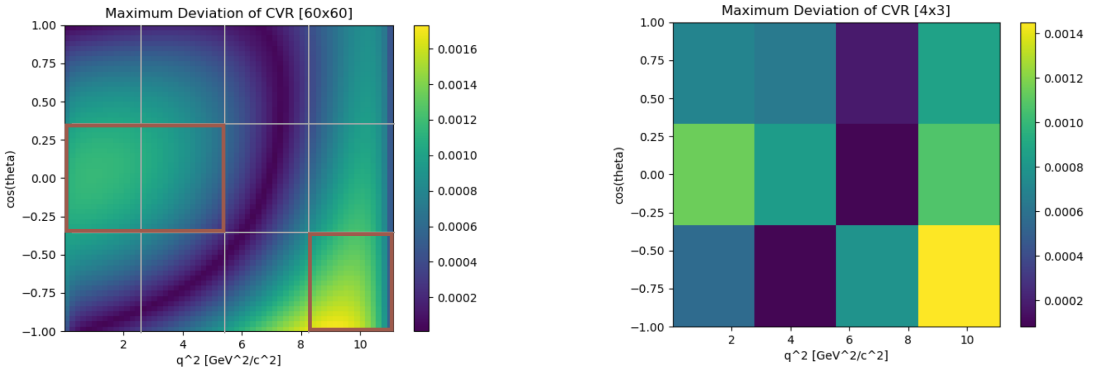

(a) Binning scheme 0 - regular 4x3.

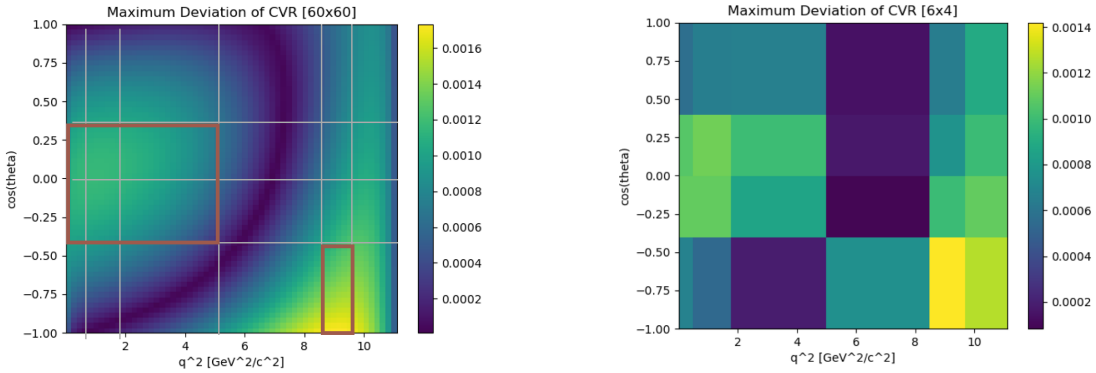

(b) Binning scheme 1 - irregular 6x4.

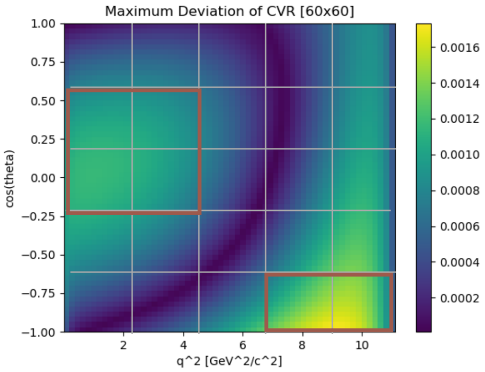

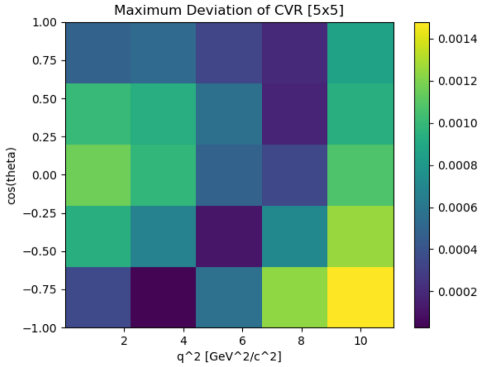

(c) Binning scheme 2 - regular 5x5.

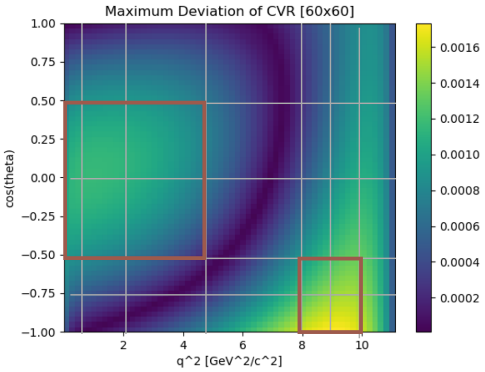

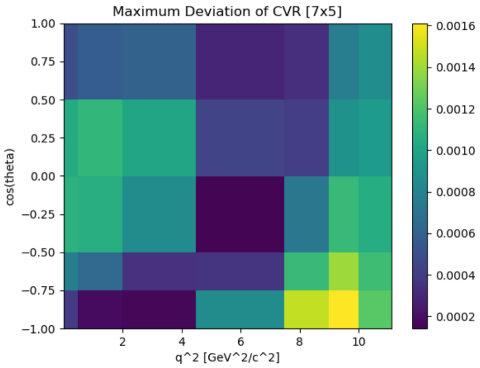

(d) Binning scheme 3 - irregular 7x5.

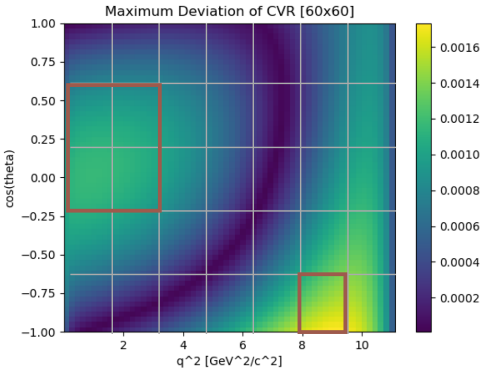

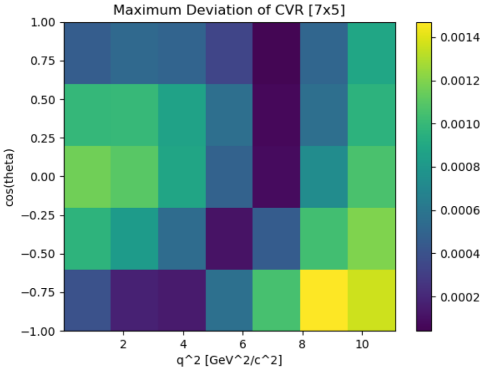

(e) Binning scheme 4 - regular 7x5.

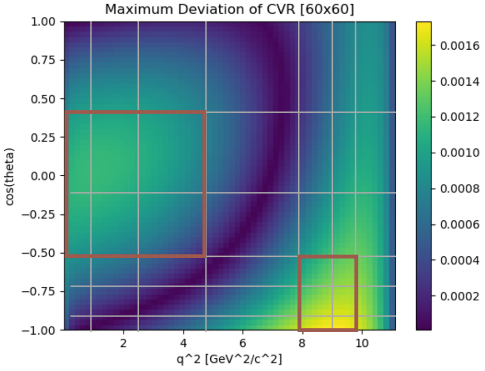

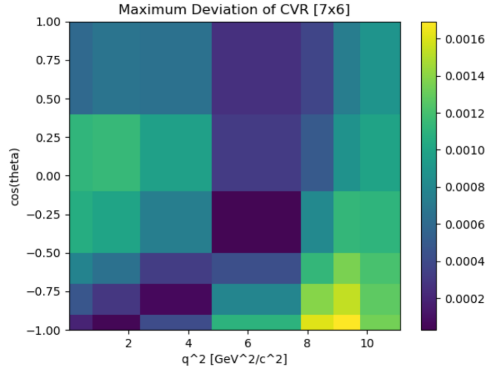

(f) Binning scheme 5 - irregular 7x6.

Figure 14: The chosen binning schemes according to the variability analysis as discussed in 4.2. The red rectangles show the region where special emphasizes was given to during the binning because of high variability.

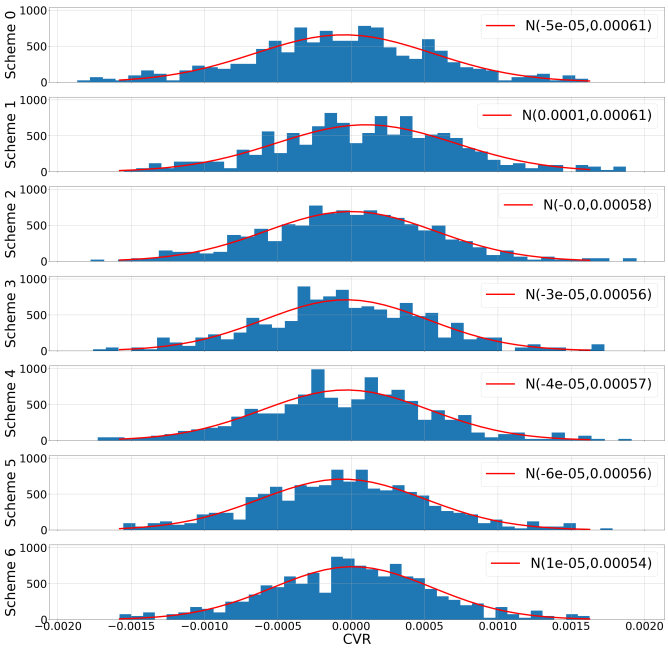

(a) CVR distribution in all binning schemes.

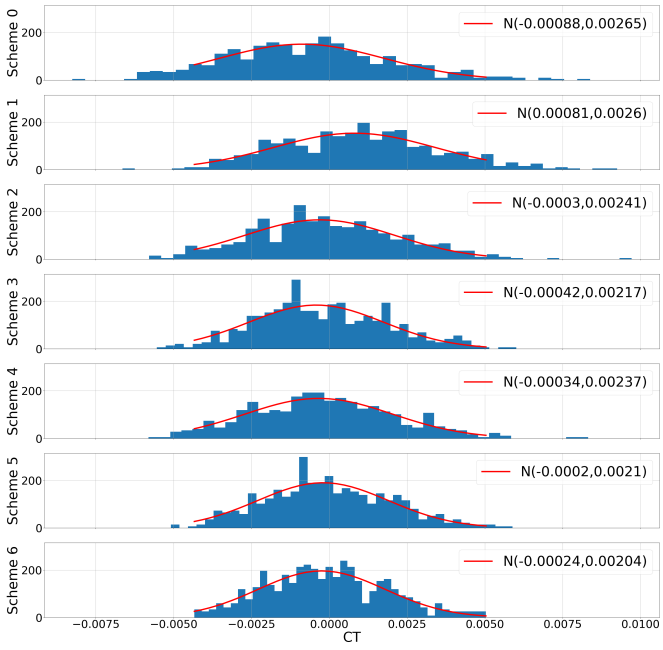

(b) CT distribution in all binning schemes.

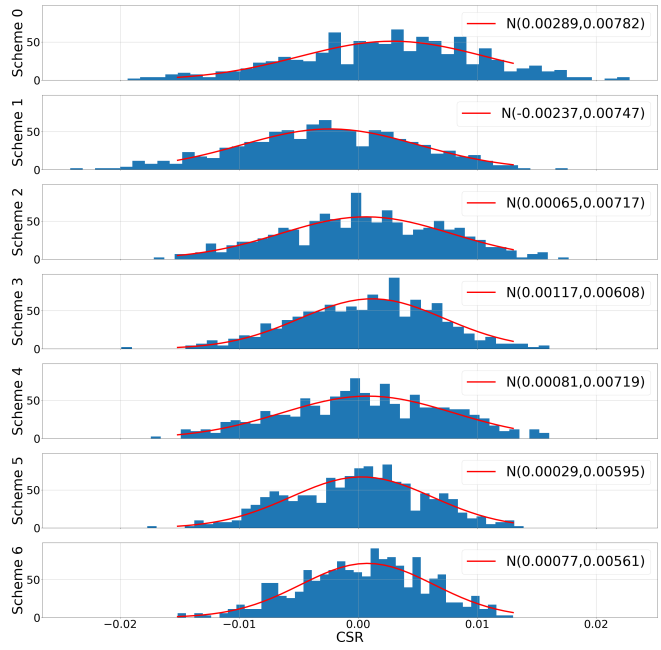

(c) CSR distribution in all binning schemes.

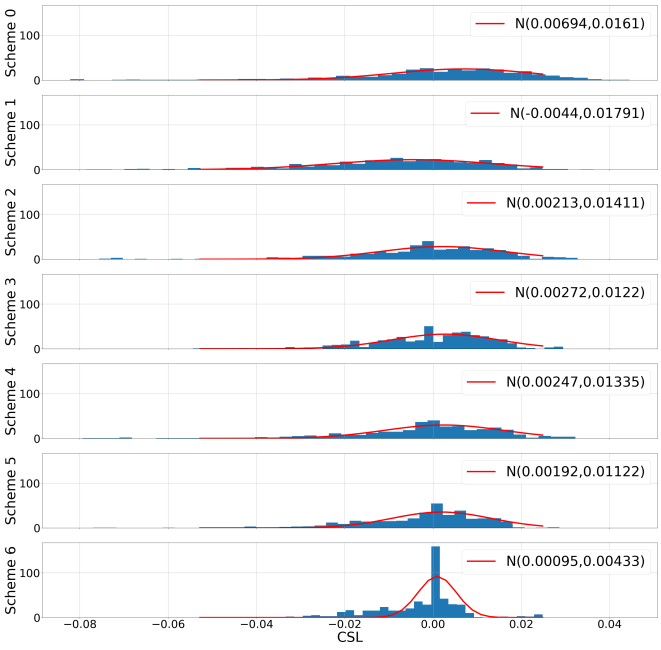

(d) CSL distribution in all binning schemes.

Figure 15: The distribution of the difference in standard model and new physics model WC values for each binning scheme with the fitted mean and standard deviation given by the function shown in red as introduced in 4.2

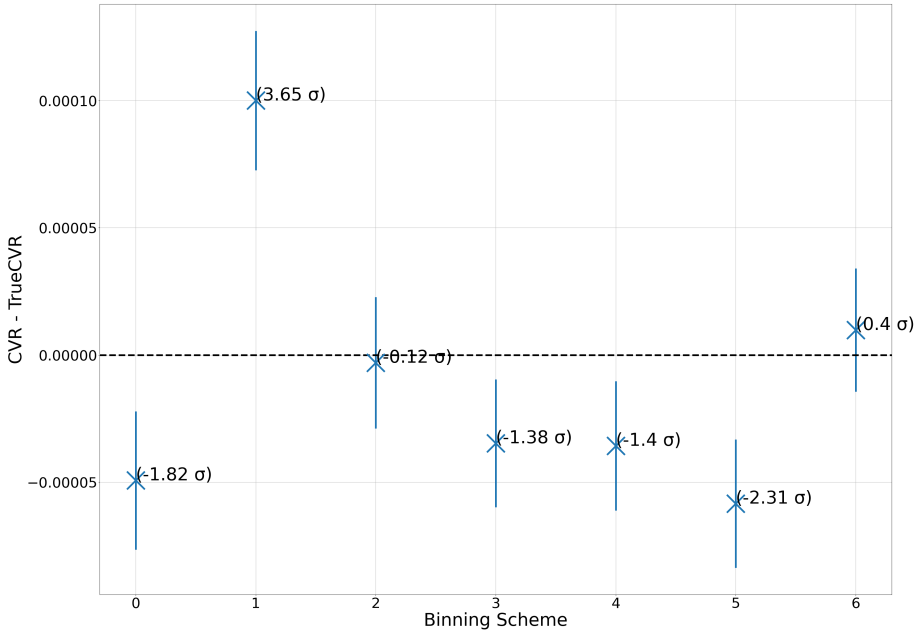

(a) CVR mean and fitted standard deviation.

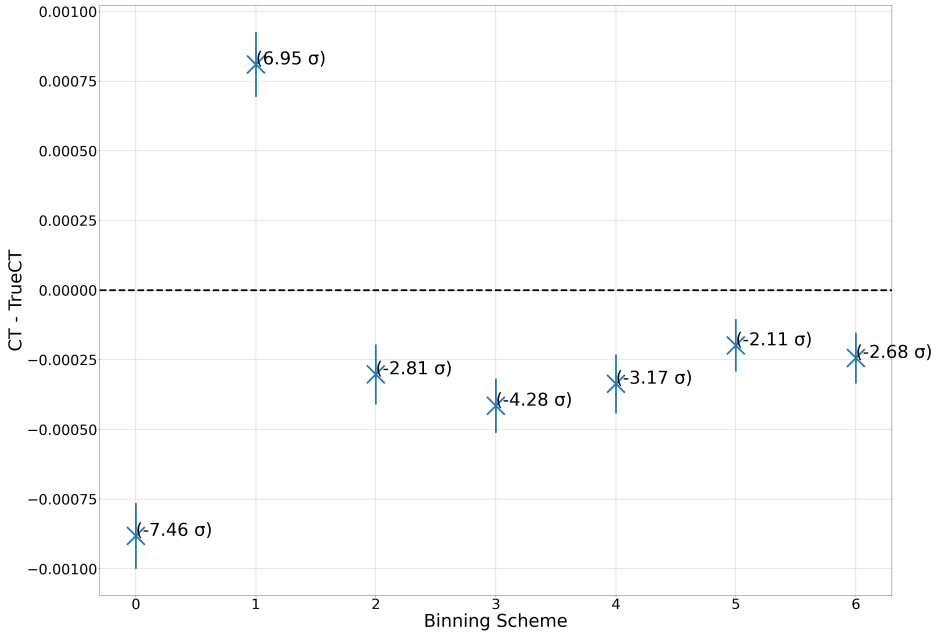

(b) CT mean and fitted standard deviation.

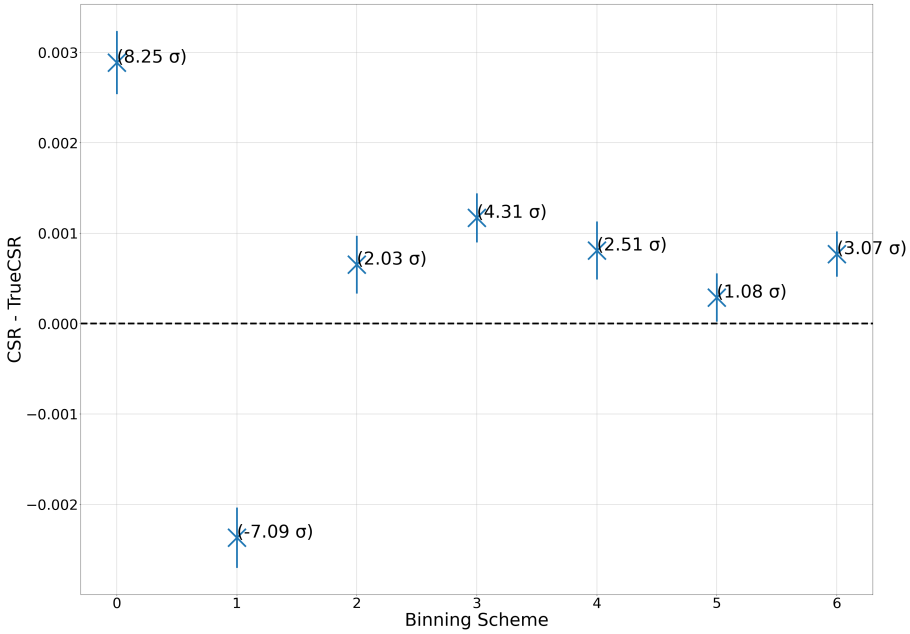

(c) CSR mean and fitted standard deviation.

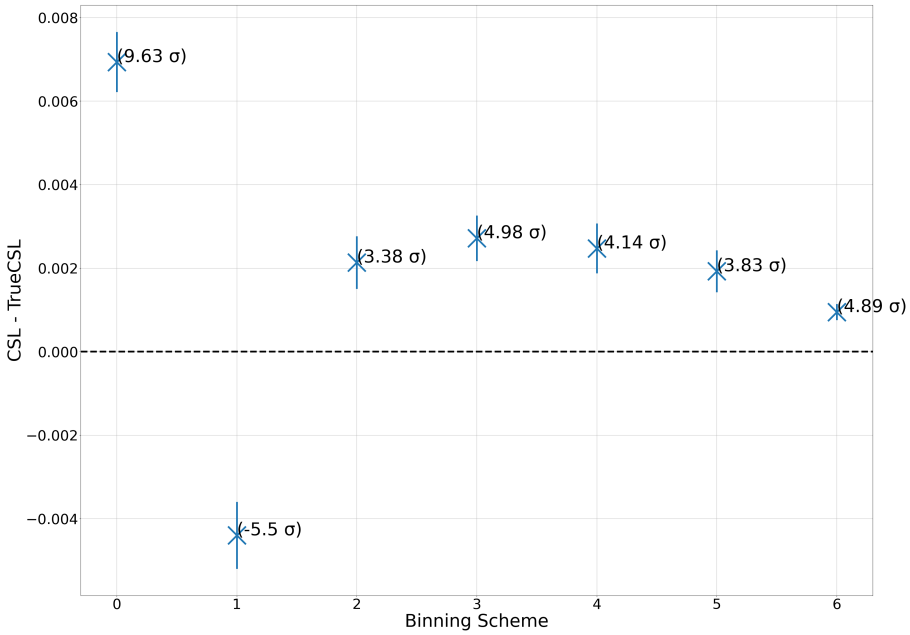

(d) CSL mean and fitted standard deviation.

Figure 16: The mean and fitted standard deviation of the WC distribution depending on the binning scheme. The uncertainty in the brackets is given by the mean divided by the standard deviation giving the probability of a value being inside the error on the mean range, where one sigma corresponds to 68% as discussed in 4.2.

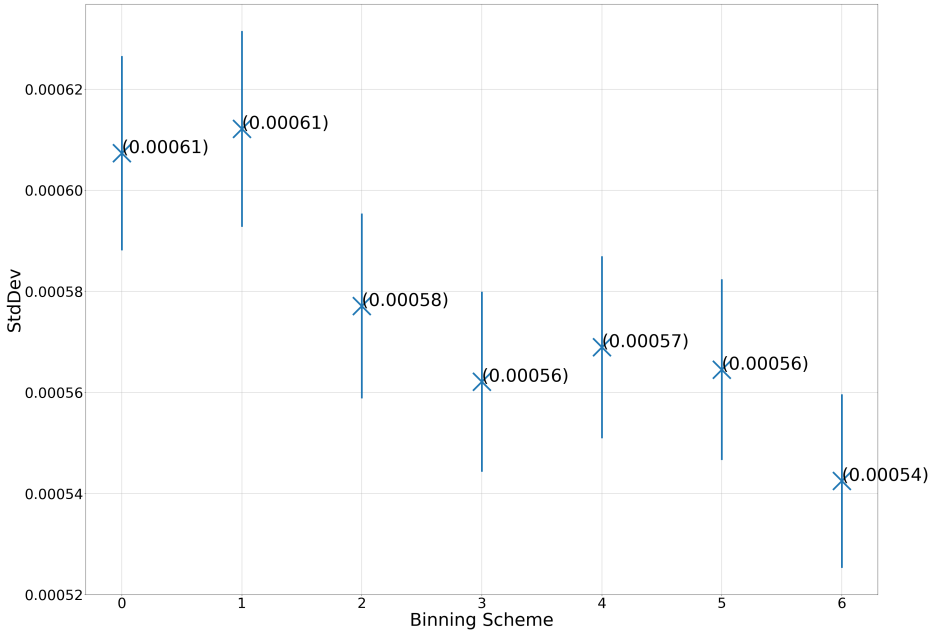

(a) CVR fitted standard deviation.

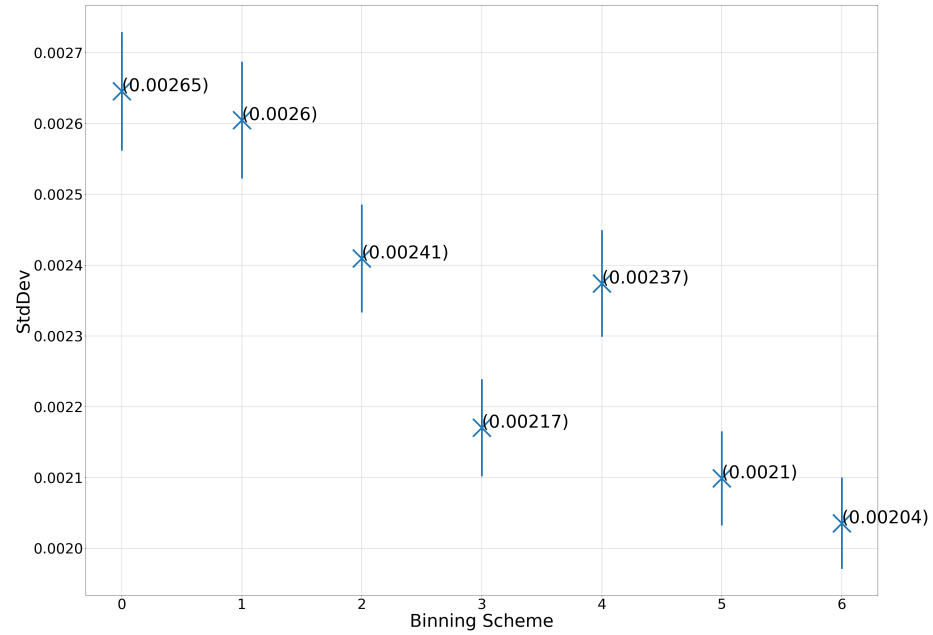

(b) CT fitted standard deviation.

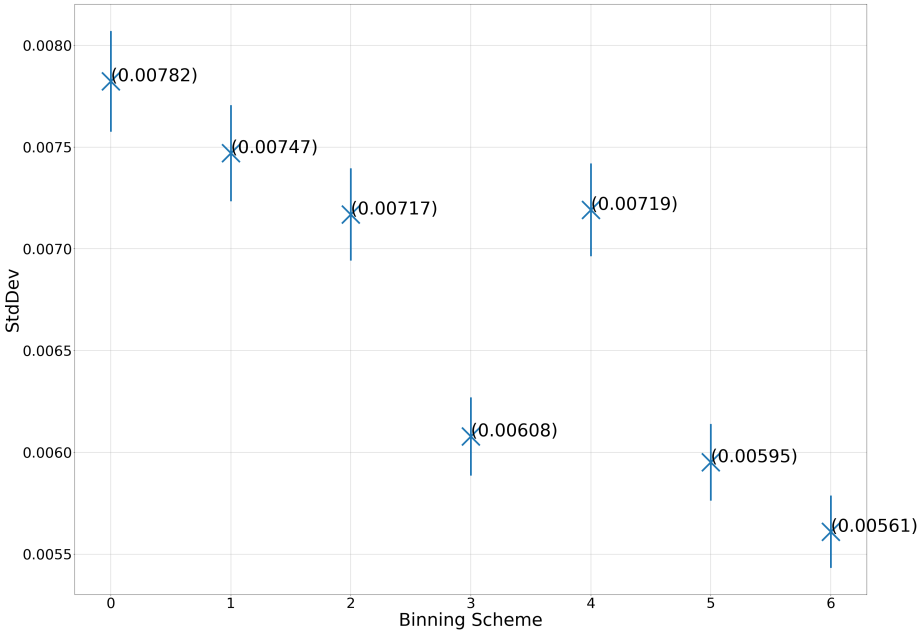

(c) CSR fitted standard deviation.

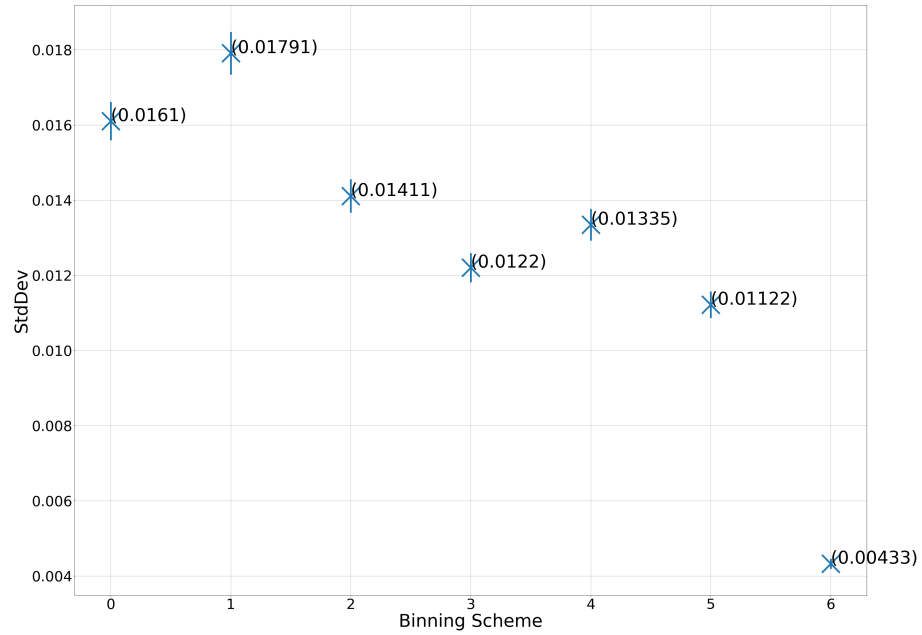

(d) CSL fitted standard deviation.

Figure 17: The estimated standard deviation depending on the binning scheme with the error calculated as in Eq. 8 as given in 4.2.

Table 4: The degradation in dependence of the binning schemes for CVR, CT, CSR and CSL for all binning schemes as discussed in 4.2.

Deg	0	1	2	3	4	5
CVR	-12.0 ± 5.0	-12.8 ± 5.1	-6.4 ± 4.8	-3.6 ± 4.6	-4.9 ± 4.7	-4.1 ± 4.7
CT	-30.0 ± 5.8	-28.0 ± 5.7	-18.4 ± 5.3	-6.6 ± 4.8	-16.6 ± 5.2	-3.1 ± 4.6
CSR	-39.4 ± 6.2	-33.2 ± 6.0	-27.8 ± 5.7	-8.3 ± 4.9	-28.2 ± 5.7	-6.1 ± 4.8
CSL	-272.3 ± 16.7	-314.1 ± 18.5	-226.3 ± 14.6	-182.1 ± 12.6	-208.6 ± 13.8	-159.3 ± 11.6

The error on the degradation δ_d was calculated using error propagation giving the following formula:

$$\delta_d = \sqrt{\left(-\frac{\delta_i}{\sigma_6}\right)^2 + \left(\frac{\sigma_i \delta_6}{\sigma_6^2}\right)^2} \tag{11}$$

with σ_i being the standard deviation and δ_i the error on the standard deviation on the i-th binning scheme.

Model Dependency Analysis

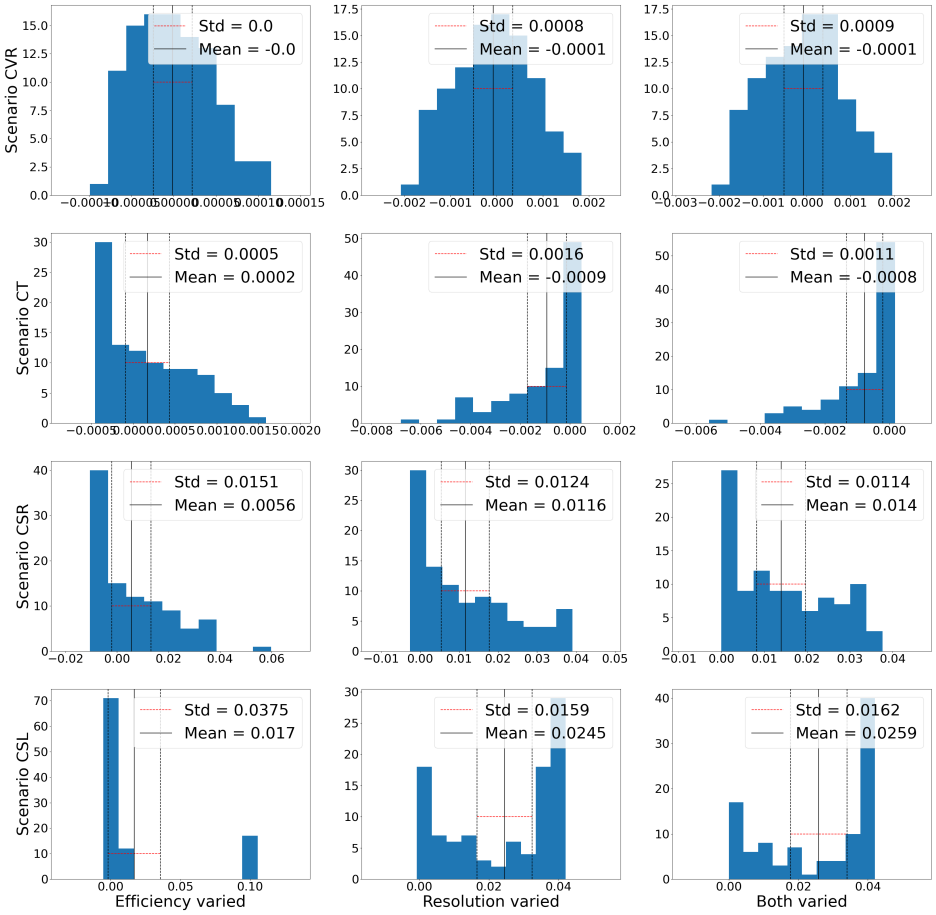

Figure 18: The WC value distributions depending on the model variations for the with the model and fit scenario set to each WC as discussed in 5.3.

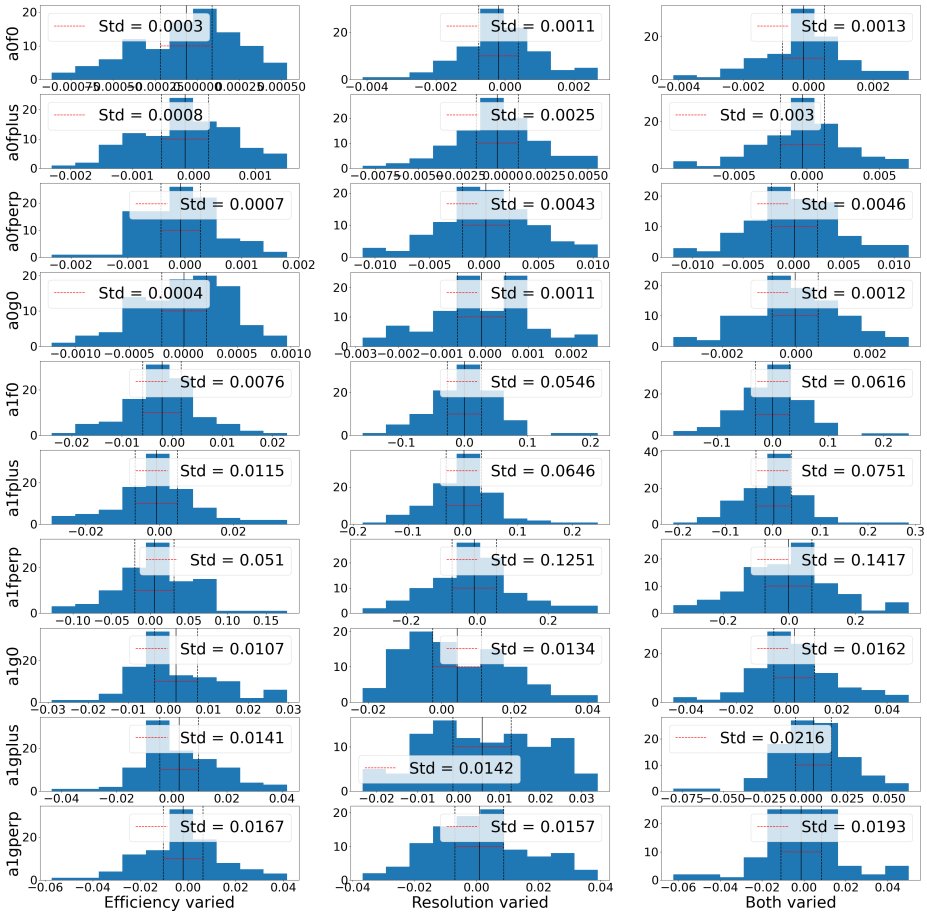

Figure 19: The FF value distributions depending on the model variations for with the model and fit scenario SM as discussed in 5.3.

References

[1] Mary K. Gaillard, Paul D. Grannis, and Frank J. Sciulli. The standard model of particle physics. *Reviews of Modern Physics*, 71, 1999.

[2] The ATLAS Collaboration. G. Aad et al. Observation of a new particle in the search for the standard model Higgs boson with the ATLAS detector at the LHC. *Physics Letters, Section B: Nuclear, Elementary Particle and High-Energy Physics*, 716, 2012.

[3] Arbey A. Mahmoudi F. Dark matter and the early universe: A review. *Progress in Particle and Nuclear Physics*, 2021, 2021.

[4] The LHCb Collaboration. R. Aaij et al. Test of lepton universality in beauty-quark decays. 2021.

[5] Martin Jung and David M. Straub. Constraining new physics in $b \to cl\nu$ transitions. *Journal of High Energy Physics*, 2019, 2019.

[6] The LHCb Collaboration. R. Aaij et al. Test of lepton universality with $\Lambda_b^0 \to pK^-l^+l^-decays$. *Journal of High Energy Physics*, 2020, 2020.

[7] P. Böer, A. Kokulu, J. N. Toelstede, and D. van Dyk. Angular analysis of $\Lambda_b \to \Lambda_c(\Lambda\pi)l\nu^-$. *Journal of High Energy Physics*, 2019, 2019.

[8] Diganta Das. Model independent new physics analysis in $\Lambda_b \to \Lambda\mu^+\mu^-$ decay. *The European Physical Journal C*, 78, 2018.

[9] Florian U. Bernlochner, Zoltan Ligeti, Dean J. Robinson, and William L. Sutcliffe. New predictions for $\Lambda_b \to \Lambda_c$ semileptonic decays and tests of heavy quark symmetry. *Physical Review Letters*, 121, 2018.

[10] Florian U. Bernlochner, Zoltan Ligeti, Dean J. Robinson, and William L. Sutcliffe. Precise predictions for $\Lambda_b \to \Lambda_c$ semileptonic decays. *Physical Review D*, 99, 2019.

[11] Aqsa Nasrullah, M. Jamil Aslam, and Saba Shafaq. Analysis of angular observables of $\Lambda_b \to \Lambda(\to p\pi)\mu^+\mu^-$ decay in the standard and Z' models. *Progress of Theoretical and Experimental Physics*, 2018, 2018.

[12] Neus Penalva, Eliecer Hernández, and Juan Nieves. Further tests of lepton flavor universality from the charged lepton energy distribution in $b \to c$ semileptonic decays: The case of $\Lambda_b \to \Lambda_c l\nu_l^-$. *Physical Review D*, 100, 2019.

[13] Ciezarek G.Franco Sevilla M.Hamilton B.Kowalewski R.Kuhr T.Lüth V.Sato Y.See. A challenge to lepton universality in b-meson decays. *Nature*, 2017, 2017.

[14] Martina Ferrillo, Abhijit Mathad, Patrick Owen, and Nicola Serra. Probing effects of new physics in $\Lambda_b^0 \to \Lambda_c^+\mu^-\bar{\nu}_\mu$ decays. *Journal of High Energy Physics*, 2019, 2019.

[15] Minoru Tanaka and Ryoutaro Watanabe. New physics in the weak interaction of $\bar{B} \to D^*\tau\bar{\nu}$. *Physical Review D - Particles, Fields, Gravitation and Cosmology*, 87, 2013.

[16] William Detmold, Christoph Lehner, and Stefan Meinel. $\Lambda_b \to pl^-\nu_l^-$ and $\Lambda_b \to \Lambda_c l^-\nu_l^-$ form factors from lattice QCD with relativistic heavy quarks. *Physical Review D - Particles, Fields, Gravitation and Cosmology*, 92, 2015.

[17] The LHCb Collaboration. A. Augusto Alves et al. The LHCb detector at the LHC. *Journal of Instrumentation*, 3, 2008.

[18] The LHCb Collaboration. R. Aaij et al. LHCb detector performance, 2015.

List of Figures

1 The Standard Model of elementary particles. 1
2 The Standard Model Feynman diagram of the Λ_b^0 decay. 3
3 Cross section through the LHCb Detector. Ref. [17] 5
4 A track reconstruction in the LHCb experiment with the five tracking stages: VELO, TT, T1-T3 in the z-x-plane, respectively in the x-y-plane in the cut-out on the top-left close to the VELO. Ref. [18] 6
5 The Cherenkov angle dependency on the momentum (left) and the setup of RICH1 (right). Ref. [17] 8
6 The schematic view of the HCAL Calorimeter Module with the WLS fibres, the PMT Photomultipliers, and the detailed view of the alternating scintillator and absorbers structure. Ref. [17] 9
7 The CVR value distributions and the Gaussian fit for different binning schemes. . 14
8 The CVR mean and fitted standard deviation. 15
9 The CVR fitted standard deviation. 15
10 The degradation of the Standard deviation on the WC value distribution in dependence of the binning schemes with respect to the control binning scheme 6 with no FF being floated. 16
11 The WC value distributions depending on the model variations with the model scenario set to SM and the fit scenario set to each WC showing the influence of the model variation in the standard model case on the fitted WC values. 20
12 The maximum sensitivity of CVR (top-left), CT (top-right), CSR (bottom-left) and CSL (bottom-right) in a 60x60 scheme as introduced in 4.1. 23
13 The maximum sensitivity of CVL in a 60x60 scheme showing a pure random fluctuation as expected as described in 4.1 24
14 The chosen binning schemes according to the variability analysis as discussed in 4.2. The red rectangles show the region where special emphasizes was given to during the binning because of high variability. 25
15 The distribution of the difference in standard model and new physics model WC values for each binning scheme with the fitted mean and standard deviation given by the function shown in red as introduced in 4.2 27
16 The mean and fitted standard deviation of the WC distribution depending on the binning scheme. The uncertainty in the brackets is given by the mean divided by the standard deviation giving the probability of a value being inside the error on the mean range, where one sigma corresponds to 68% as discussed in 4.2. 29
17 The estimated standard deviation depending on the binning scheme with the error calculated as in Eq. 8 as given in 4.2. 31
18 The WC value distributions depending on the model variations for the with the model and fit scenario set to each WC as discussed in 5.3. 33
19 The FF value distributions depending on the model variations for with the model and fit scenario SM as discussed in 5.3. 34

List of Tables

1 The selected binning schemes and their regularity with Scheme 6 being the control binning. 13
2 The degradation in dependence of the binning schemes 2 and 5 for CVR, CT, CSR and CSL. 16
3 The five model scenarios with either the FFs or the WCs varied. 18
4 The degradation in dependence of the binning schemes for CVR, CT, CSR and CSL for all binning schemes as discussed in 4.2. 32